Silicate Weathering in the Semi-Arid Southern Pyrenees During the PETM: Lithium Isotope Evidence

Rocio Jaimes-Gutierrez[1], Marine Prieur[1], David J. Wilson[2], Philip A.E. Pogge von Strandmann[2, 3], Emmanuelle Pucéat[4], Thierry Adatte[5], Jorge E. Spangenberg[6], Sébastien Castelltort[1]

[1] Department of Earth Sciences, University of Geneva, Rue des Maraîchers 13, 1205, Geneva, Switzerland
[2] London Geochemistry and Isotope Centre (LOGIC), Institute of Earth and Planetary Sciences, University College London and Birkbeck, University of London, Gower Street, London WC1E 6BT, UK
[3] Institute of Geosciences, Johannes Gutenberg University Mainz, Mainz, Germany
[4] Biogéosciences Dijon, Université Bourgogne Franche – Comté, UMR CNRS 6282, Dijon, France.
[5] Institute of Earth Sciences, Géopolis, University of Lausanne, 1015 Lausanne, Switzerland
[6] Institute of Earth Surface Dynamics, Géopolis, University of Lausanne, 1015 Lausanne, Switzerland

Correspondence to: Rocio Jaimes-Gutierrez, Rocio.JaimesGutierrez@unige.ch

Abstract

The Palaeocene-Eocene Thermal Maximum (PETM), a hyperthermal event ~56 Ma ago, allows the Earth system response to abrupt climate change to be explored. Recent investigations link the PETM with a negative lithium isotope (δ^7Li) excursion, interpreted as an increase in continental silicate weathering fluxes, which can regulate Earth's surface temperature over geological timescales. However, the silicate weathering response under different climatic regimes has yet to be constrained. Here we aim to address the chemical weathering response to the PETM in the semi-arid Southern Pyrenees, and to explore how different archives (i.e. clays and carbonate nodules) record the weathering changes.

We investigated two continental sections in the southern Pyrenees. In the Esplugafreda section, we measured δ^7Li values as a silicate weathering proxy and ϵ_{Nd} values as a provenance proxy in the clay minerals. In the Rin section, we characterised the PETM locally by analysing $\delta^{13}C$ values in organic matter and examined the clay mineralogy in the paleosols, as well as measuring δ^7Li values in clays and carbonate nodules to trace silicate weathering. In the Esplugafreda section, we observe temporally stable ϵ_{Nd} values, while the δ^7Li_{clays} record shows two small positive excursions, one during the Pre-Onset Excursion (~0.7‰) and a second during the body of the PETM (~0.8‰). In the Rin section, the PETM is characterised by a negative carbon isotope excursion of 2.8‰. The clays consist mostly of illite/smectite, illite, kaolinite, and chlorite consistent with a seasonal climate in the region, and we find a positive δ^7Li_{clays} excursion of ~0.8‰.

The combined δ^7Li_{clays} and ϵ_{Nd} records indicate increased clay formation and increased silicate weathering fluxes in the semi-arid Pyrenees, while the sediment provenance was stable. The δ^7Li values in the carbonate nodules indicate more variability, potentially due to clay contamination. Constrained by the bedrock type of dominantly reworked sediments and the seasonal precipitation regime, the initially low weathering fluxes, despite a comparatively high weathering intensity, evolved towards higher weathering fluxes with enhanced erosion during the PETM.

Short Summary

How do semi-arid landscapes respond to rapid global warming? During the PETM – an extreme warming event 56 Ma ago – global lithium isotope records show a negative δ^7Li excursion, suggesting an increase in weathering fluxes. In the Southern Pyrenees, however, we find the opposite signal: clay δ^7Li values became ~1‰ heavier, indicating enhanced clay formation. These results suggest that regional hydroclimatic conditions can decouple terrestrial signals from global averages.

1.   Introduction

Continental silicate weathering is a critical feedback mechanism that stabilises Earth's climate over geological timescales by regulating atmospheric CO_2 through the long-term carbon cycle (Walker et al., 1981; Raymo and Ruddiman, 1992; Maher and Von Blanckenburg, 2023). Through the breakdown of silicate minerals, the transport of cations in river systems, and the precipitation and burial of carbonates in the ocean, silicate weathering sequesters atmospheric CO_2, acting as a natural climate thermostat. Understanding how this process responds to abrupt climate change is essential for evaluating its capacity to modulate carbon fluxes under a range of future warming scenarios.

The Palaeocene-Eocene Thermal Maximum (PETM), a hyperthermal event ~56 Ma ago, resulted from the rapid release of greenhouse gases that triggered a 5–8 °C global temperature increase over a geologically brief interval (Kennett and Stott, 1991; Dickens et al., 1995; Zachos et al., 2003, 2008; Westerhold et al., 2009; McInerney and Wing, 2011). Global records from the PETM suggest increases in silicate weathering fluxes (e.g. Hessler et al., 2017; Pogge von Strandmann et al., 2021; Jaimes-Gutierrez et al., 2025; Rush et al., 2025), while some local records have been interpreted to show increased weathering intensity (e.g. Ramos et al., 2022; Chen et al., 2023), underscoring the potential for weathering to buffer atmospheric CO_2 during extreme warming events. In the context of modern anthropogenic warming, these insights are crucial for understanding the capacity of natural systems to mitigate rising CO_2 levels (Zeebe et al., 2016; Carmichael et al., 2017 and references therein).

In mid-latitude records, a range of sedimentological, geochemical, and mineralogical proxies suggest that the PETM resulted in a hydrological perturbation with episodic extreme rainfall events, increased seasonality, and aridification, leading to a loss of vegetation, extreme flooding, and enhanced channel mobility (Schmitz et al., 2001; Schmitz and Pujalte, 2007; Carmichael et al., 2017; Chen et al., 2018; Rush et al., 2021; Barefoot et al., 2022; Vimpere et al., 2023). These changes were particularly pronounced in semi-arid regions such as the Southern Pyrenees (~35ºN paleolatitude, **Fig. 1**), where sedimentary records document hydrological seasonality, enhanced erosion, and increased sediment transport (Schmitz and Pujalte, 2007; Pujalte et al., 2015; Chen et al., 2018; Rush et al., 2021; Prieur et al., 2024, 2025; Jaimes-Gutierrez et al., 2024).

The Southern Pyrenees (**Fig. 1**) offer an exceptional setting for investigating climate-driven weathering dynamics. This region experienced tectonic quiescence during the PETM (Rosenbaum et al., 2002), allowing for the isolation of the effects of climate and hydrology on weathering. Sedimentary records indicate enhanced hydrological seasonality and increased runoff, consistent with amplified denudation rates during this interval (Schmitz and Pujalte, 2007; Pujalte et al., 2015; Rush et al., 2021). In this study, we use lithium isotopes (δ^7Li) as a proxy for silicate weathering and neodymium isotopes (ε_{Nd}) as a tracer for sediment provenance, in order to quantify the weathering responses in the Southern Pyrenees and to assess their regional contribution to CO_2 regulation during the PETM.

We focus on two continental floodplain sections to answer two primary questions: (i) What was the chemical weathering response to the PETM in the semi-arid Southern Pyrenees? (ii) How do different sedimentary archives, such as clays and carbonate nodules, record the weathering changes? In the Esplugafreda section, we measured δ^7Li values in clay minerals as a weathering proxy, together with ε_{Nd} values in two clay size fractions to determine sediment provenance. In the Rin section, we characterised the PETM locally through δ^{13}C measurements in organic matter, and analysed the clay mineralogy of paleosols, and δ^7Li values in both clays and carbonate nodules. These geochemical and mineralogical datasets allow us to reconstruct weathering dynamics in the region and to assess how they compare with existing globally-distributed records of PETM weathering (Pogge von Strandmann et al., 2021b; Ramos et al., 2022; Chen et al., 2023; Jaimes-Gutierrez et al., 2025a; Rush et al., 2025).
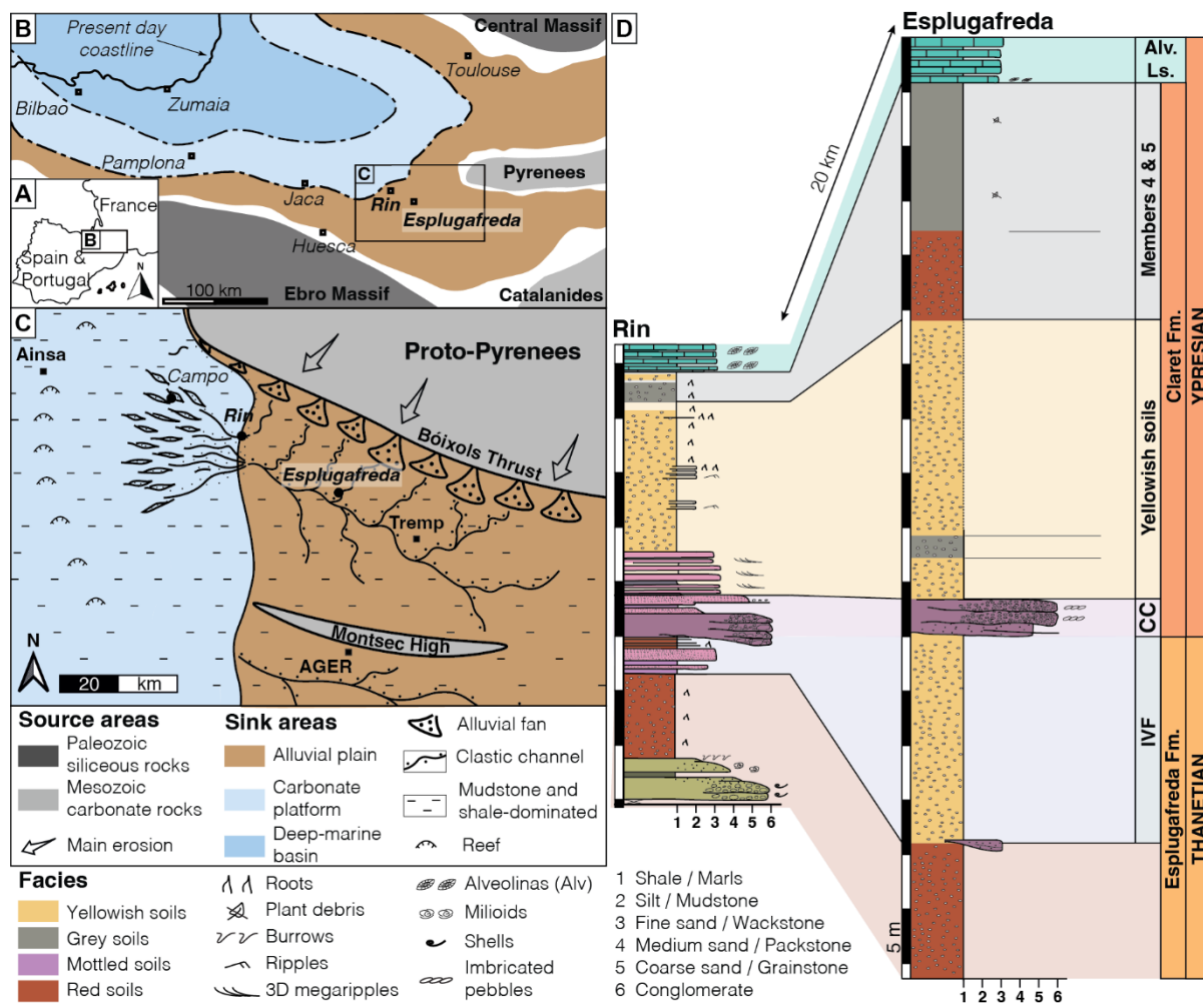
Figure 1. *(A) Location map. (B) Palaeogeography of the Tremp-Graus Basin during the late Palaeocene, modified after Jaimes-Gutierrez et al. (2024) and references therein. (C) Sediment routing system during the late Palaeocene, with the floodplain Esplugafreda section and the more coastal Rin section, at the marine-continent transition, modified from Prieur et al. (2025). (D) Stratigraphy and correlation between the Esplugafreda and Rin terrestrial sections. CC, Claret Conglomerate. Alv. Ls., Alveolina Limestone.*

1.1.   Silicate weathering as Earth's surface thermostat

Silicate weathering rates are influenced by climate (Dessert et al., 2003; West et al., 2005), vegetation (Moulton et al., 2000; Porder, 2019), lithology (Dessert et al., 2003; Caves et al., 2016; Murray and Jagoutz, 2024), and regolith properties (Kump and Arthur, 1997; Caves Rugenstein et al., 2019). Weathering is driven by the availability of fresh mineral surfaces, reactive fluids, and dissolution kinetics (Riebe et al., 2004; Bufe et al., 2021; Maher and Von Blanckenburg, 2023). Denudation (D = erosion rate [E] + silicate weathering [W]) links surface processes to the carbon cycle because erosion supplies fresh minerals, enhancing CO_2 sequestration through chemical weathering (Gaillardet et al., 1999; Riebe et al., 2004; West et al., 2005; Anderson et al., 2007; Hilton, 2023).

Two end-member regimes can be used to describe chemical weathering dynamics. In supply-limited regimes, mature soils dominated by secondary clays shield bedrock, limiting fresh mineral exposure and resulting in low weathering rates (Goddéris et al., 2008). In kinetically-limited regimes, which are typical of high-relief areas with thin soils, weathering rates are controlled by mineral dissolution kinetics (Kump et al., 2000; Riebe et al., 2004; West et al., 2005). Investigating how climate and erosion interact to shape these regimes under hyperthermal events such as the PETM is thus essential for understanding the weathering mechanisms and rates underpinning Earth's carbon cycle feedbacks in a warming climate.

1.2.   Lithium isotopes as a chemical weathering tracer

Secondary clay minerals, which form as a by-product of primary silicate rock dissolution, preferentially incorporate ^{6}Li over ^{7}Li, resulting in isotopically light clays and isotopically heavy waters (e.g. Pogge von Strandmann et al., 2020). As weathering progresses, both dissolved lithium and the clays that precipitate from it become isotopically heavier, with the δ^7Li value of the water and soil being linked by an approximately constant fractionation factor (Pogge von Strandmann et al., 2021a). Measuring δ^7Li values in detrital and carbonate archives therefore allows past weathering regimes to be reconstructed. Because carbonate weathering has a minimal influence on riverine lithium budgets, δ^7Li variations primarily reflect silicate weathering processes (Kısakűrek et al., 2005). Consequently, lithium isotopes have become widely applied as a proxy for tracking clay mineral formation, and thereby tracing silicate weathering intensity changes, both in modern systems (e.g. Dellinger et al., 2015, 2017; Pogge von Strandmann et al., 2023) and during past geological events (e.g. Misra and Froelich, 2012; Pogge von Strandmann et al., 2013, 2021; Ramos et al., 2022; Jones et al., 2023).

Weathering congruency, which represents the balance between primary mineral dissolution and secondary clay mineral formation, determines the δ^7Li composition of river waters and sediments (Dellinger et al., 2015; Zhang et al., 2022 and references therein). In rapidly eroding regions with low *W/D*, congruent weathering results in minimal isotopic fractionation, because clay formation is relatively low (**Fig. 2**). In contrast, incongruent weathering in soil-mantled environments with moderate *W/D*, such as floodplains with high clay formation, yields both clays and waters with higher δ^7Li values (**Fig. 2 and 3**). Finally, in supply-limited regimes with high *W/D*, such as rainforests, there is no remaining primary rock material to weather, so pre-formed clays are re-dissolved, which drives solutions to low δ^7Li values, but with a very low weathering flux (e.g. Dellinger et al., 2015). In modern rivers, clays take up their Li from solution with an approximately constant fractionation factor (Pistiner and Henderson, 2003; Pogge von Strandmann et al., 2023; Ramos et al., 2024), so their composition also mimics this boomerang curve (Winnick et al., 2022; Pogge von Strandmann et al., 2023; Wei et al., 2025).

In detrital sediment archives, only part of this boomerang trend is typically observed because of mixing of the neoformed clays with primary silicate material, especially at low *W/D* conditions (Dellinger et al., 2017). Therefore, continental and marine detrital records may need to be interpreted differently (e.g. Pogge von Strandmann et al., 2021; Ramos et al., 2022, 2024; Jones et al., 2023; Jaimes-Gutierrez et al., 2025; Rush et al., 2025; Wei et al., 2025). Because finer sediment fractions tend to be preferentially transported further offshore due to hydrodynamic sorting during river to marine transport, clay-sized records may be more clearly expressed in some marine sedimentary records (e.g. Gibbs, 1977; Liu et al., 2023). Such biases resulting from mixing with primary silicate grains in bulk sediment samples can potentially be reduced by analysing the clay size fraction (<2 μm), although this fraction can still also contain some primary minerals.

Finally, lithium isotopes can also be fractionated by direct climatic fluctuations. For example, temperature (Vigier et al., 2008; Li and West, 2014) and hydrological controls (Zhang et al., 2022) have both been found to influence the δ^7Li composition of river water, and consequently the composition of the sedimentary archives that form in equilibrium with them (Pogge von Strandmann et al., 2023). In particular, riverine dissolved δ^7Li values have been shown to have a negative correlation with runoff, because it controls the water-rock residence time that affects clay formation, with the dry season exhibiting enhanced clay formation and higher δ^7Li values than the wet season (Wilson et al., 2021; Zhang et al., 2022).

A detailed discussion on the lithium isotope interpretative framework. including the roles of grain size, hydrodynamic sorting, and lithology, is provided in Jaimes-Gutierrez et al. (2025, Supplemental Material).
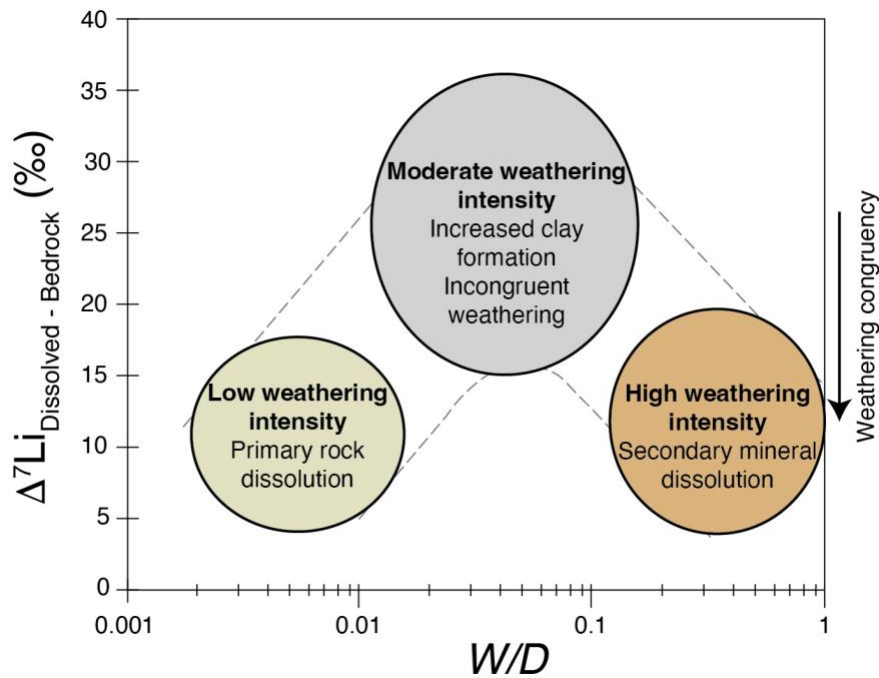
Figure 2. Large-river dissolved lithium isotope composition ($\delta^7Li_{dissolved}$) corrected for bedrock composition ($\Delta^7Li_{dissolved-bedrock}$) plotted versus weathering intensity (W/D). Modified from Dellinger et al. (2015) and references therein.

During the PETM, Pogge von Strandmann et al. (2021) documented a ~3‰ negative δ^7Li excursion in several marine carbonate sections, indicating globally enhanced weathering fluxes (50–60%) and erosion rates (2-3x), and a shift to an overall lower weathering intensity regime. At a continental scale, detrital lithium isotope records from North America show coherent negative δ^7Li excursions in both floodplain and deep-marine settings, indicating rapid propagation of erosion- and weathering-related signals through sediment-routing systems under intensified hydrological conditions, despite largely stable sediment provenance (Ramos et al., 2022; Jaimes-Gutierrez et al., 2025a; Rush et al., 2025). On a regional scale, Ramos et al. (2022) reported a rapid, sustained increase in silicate weathering intensity in the Bighorn Basin floodplains that was attributed to seasonal hydrological variability. Similarly, Chen et al. (2023) identified a ~100% increase in silicate weathering intensity in the Nanyang Basin, East Asia. These studies highlight the roles of local hydrology, lithology, and erosion in shaping regional weathering responses and the associated δ^7Li changes. However, they also reveal significant gaps in our understanding of how regional processes integrate into driving global δ^7Li records and carbon cycle feedbacks. Notably, discrepancies between the proposed increases in weathering intensity at a regional scale (Ramos et al., 2022; Chen et al., 2023) and the inferred decrease at a global scale (Pogge von Strandmann et al., 2021b; Jaimes-Gutierrez et al., 2025a; Rush et al., 2025) require further assessment of how regional climatic and geological controls translate into weathering responses.
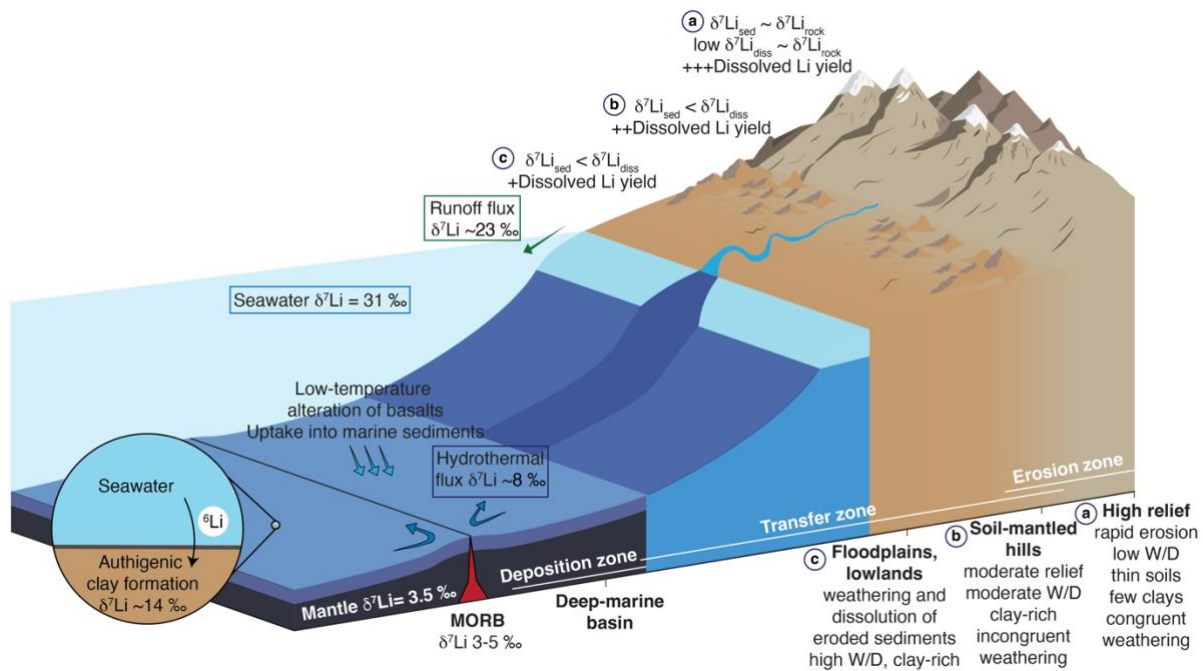
Figure 3. *Processes determining the lithium isotope composition of bulk sediments (δ^7Li_{sed}) and dissolved lithium flux along a sediment routing system from source to sink in relation to denudation. The weathering intensity (W/D) expresses the relative share of weathering (W) over denudation (D), where D = W + E (erosion). Modified from Tofelde et al. (2021), Pogge von Strandmann et al. (2021a), and Bufe et al. (2024).*

To address these gaps, we focused on the silicate weathering response to the PETM climatic perturbation in two sections of the Southern Pyrenees (Espugafreda and Rin, **Fig. 1**). With its semi-arid climate, seasonal precipitation, and relatively unreactive lithologies comprising reworked sediments and significant carbonate content (e.g. Eichenseer, 1988; Eichenseer and Luterbacher, 1992; Gómez-Gras et al., 2016), this setting represents a contrasting regional weathering regime to previous PETM studies. Our results contribute to understanding how floodplain paleosols, which are often overlooked in global weathering studies, respond to climatic perturbations, with broader implications for the recovery of Earth's climate system after significant warming events.

2. Geological context

The Pyrenees formed as a result of convergence between the Iberian and European plates, a process that initiated in the Late Cretaceous and continued into the Miocene (Mattauer and Henry, 1974; Roure et al., 1989; Roest and Srivastava, 1991; Rosenbaum et al., 2002). The orogenic evolution began with the mid-Cretaceous hyper-extension of the Iberian margins, followed by the late Cretaceous subduction and collision with the European plate (Teixell et al., 2016). Foreland basins formed on both sides of the fold and thrust belt (Puigdefbregas and Souquet, 1986; Muñoz, 1992; Gómez-Gras et al., 2016). The Southern Pyrenean foreland basin was active between the Late Cretaceous and the Oligocene, and contains well-preserved sedimentary archives of continental and marine environments.

The Tremp-Graus Basin is located in the South-Central Pyrenean Foreland Basin (Spain), delimited by the Boixols Thrust to the north and the Montsec Thrust to the south (**Fig. 1C**). During the Palaeocene, the Tremp-Graus Basin was dominated by continental sedimentation sourced from the Pyrenees (Gómez-Gras et al., 2016). The continental deposits of the Thanetian Esplugafreda Formation (Fm.) predominantly represent floodplain sediment accumulation and consist of clay, silt, carbonate nodules, and Microcodium grains, with some isolated sandy to conglomeratic channels (Puigdefbregas and Souquet, 1986; Dreyer, 1993; Schmitz and Pujalte, 2003, 2007).

2.1. Esplugafreda section

The Esplugafreda section (42º14'50" N; 0º45'13" E, **Fig. 1B**) has been widely studied for its well-preserved Palaeocene-Eocene sedimentary record (Schmitz and Pujalte, 2003; Baceta et al., 2005; Khozyem, 2013; Tremblin et al., 2022; Basilici et al., 2022; Jaimes-Gutierrez et al., 2024) (**Fig. 1D**). The Upper Thanetian sediments belong to the Esplugafreda Fm. in the Tremp Group of the Tremp-Graus Basin (Dreyer, 1993). This formation consists of coarse-grained stream deposits intercalated with red floodplain sediments that are rich in carbonate nodules and characterised by mature paleosols. The PETM sediments have been classified into five stratigraphic members

(Pujalte and Schmitz, 2005; Pujalte et al., 2014; Colombera et al., 2017; Basilici et al., 2022). Member 1 belongs to the Esplugafreda Fm. and consists of a fining-upwards sequence of conglomerates and cross-laminated sandstones, known as the Incised Valley Fill (IVF) sediments. During this interval, a first negative carbon isotope excursion (CIE) marks the Pre-Onset Excursion (POE) (Khozyem, 2013; Tremblin et al., 2022). Member 2 at the onset of the Ypresian is represented by the Claret Conglomerate (Pujalte and Schmitz, 2005), a 3-5 m thick conglomeratic unit, corresponding to a braid plain which has been interpreted as the proximal part of a megafan (Schmitz and Pujalte, 2007). Member 3, the Yellowish soils, consists of yellow mudstone with purple mottling, and the main body of the CIE is recorded during this interval (Pujalte and Schmitz, 2005). Member 4, consisting of red soil with gypsum, and Member 5, comprising light red mudstones with scarce carbonate nodules, correspond to the recovery interval of the PETM in this locality (Pujalte and Schmitz, 2005; Baceta et al., 2011; Khozyem, 2013; Pujalte et al., 2014; Tremblin et al., 2022; Basilici et al., 2022).

2.2. Rin section

The Rin section (42°19'42.01"N; 0°32'42.16"E, **Fig. 1B and Fig. 4**) is a Palaeocene-Eocene sequence comprising mudstone-dominated alluvial deposits and very shallow marine carbonate alternations, indicating episodes of transgression and regression on the coastal plain (Schmitz and Pujalte, 2007) (**Fig. 1**). The upper Esplugafreda Fm. soils are characterised by grey mottling and sparse iron nodules, with preserved pedogenic features such as peds. Member 1, the IVF, consists of 4 m-thick reddish-yellow soils that are rich in carbonate nodules. Member 2, the Claret Conglomerate, outcrops as a 3 m-thick calcareous conglomerate with pale red clay pockets, and has sparse carbonate nodules and charophyte occurrences. Member 3, the Yellowish soils, consists of 13 m-thick reddish-yellow clays and silts. The base of Member 3 records sparse occurrences of lignite and carbonate nodules. Member 4 is not preserved in the Rin section, and the upper 3 m of the sequence consists of Member 5, which has light grey to reddish yellow soils with grey mottling, before the overlying Alveolina Limestone.

Figure 4. Rin section between the upper Thanetian and lower Ypresian. Members 1-5 described in the literature for the Esplugafreda section can be identified in the Rin section, except that Member 4 from the recovery phase of the PETM has not been preserved. E. Fm.: Esplugafreda Formation.

3. Material and methods

3.1. Size fraction separation

Standard protocols (e.g. Adatte et al., 1996; Bauer et al., 2016) were followed for decarbonation and size fraction separation at the Institute of Earth Sciences clay laboratory at the University of Lausanne (ISTE-UNIL). Samples (~5 g) were leached with 10% HCl for 30 min in a bubble bath, including 3 min in an ultrasonic bath, to disaggregate sediments and dissolve calcite. Distilled water was used to remove the acid until a neutral pH was obtained. Subsequently, the <2 µm fraction was separated by settling and enhanced with a centrifuge. Settling and extraction were repeated three times.

3.2. Clay mineralogy

The clay minerals were identified on air-dried and ethylene glycol-solvated samples at ISTE-UNIL following the protocol described in Adatte et al. (1996). An aliquot of the separated size fractions was pipetted on glass slides and dried at room temperature. The air-dried samples were further analysed with a Thermo Scientific ARL X'TRA powder diffractometer equipped with a Cu anode, operated at 45 kV and 40 mA. The step size was 0.02 °, with a scan rate of 0.5-1.2 °/min. Samples were glycolated to identify smectite (Moore and Reynolds, 1992). Diffractograms were analysed using the XRDWin software, where the background was removed, and a deconvolution was performed for overlapping peaks (e.g. K002 and Ch004).

7

3.3. Nodule purification

Carbonate nodules were washed with running distilled water until visible clay clumps were removed. They were then placed in a beaker with distilled water and in an ultrasonic bath to remove the remaining clay particles. A second round in the ultrasonic bath was then carried out with some drops of 10 M HCl in order to remove the outermost layer. The nodules were later washed in running distilled water, dried at 40 ºC, and ground.

3.4. Rock-Eval pyrolysis

Organic matter analyses were performed on powdered bulk rock samples using a Rock-Eval 6 at ISTE-UNIL, following standard methodology (Espitalie et al., 1985; Behar et al., 2001). For calibration, the IFP 160000 standard was used. The Rock-Eval pyrolysis parameters measured were hydrogen index (HI, mg HC/g TOC, HC = hydrocarbons), oxygen index (OI, mg CO_2/g TOC), Tmax (°C), and total organic carbon content (TOC, wt.%). The HI, OI, and Tmax values give an overall measurement of the type and degree of maturation of the organic matter (e.g. Espitalie et al., 1985).

3.5. Isotope geochemistry

3.5.1. Organic matter carbon isotopes

The carbon isotope composition of the decarbonated bulk rock samples was determined at the Institute of Earth Surface Dynamics at the University of Lausanne (IDYST-UNIL) by elemental analysis/isotope ratio mass spectrometry (EA/IRMS). The EA/IRMS system consisted of a Carlo Erba 1108 (Fisons Instruments, Milan, Italy) elemental analyser connected to a Delta V Plus isotope ratio mass spectrometer via a ConFlo III split interface (both Thermo Fisher Scientific, Bremen, Germany) operated under continuous helium (He) flow (Spangenberg, 2006; Spangenberg and Zufferey, 2019). The carbon isotope compositions were reported in the delta (δ) notation as permil (‰) variations of the molar ratio of the heavy to light isotope ($^{13}C/^{12}C$) relative to the international standard Vienna Pee Dee Belemnite limestone (VPDB). For calibration and normalisation of the measured $\delta^{13}C$ values to the Vienna Pee Dee Belemnite limestone (VPDB) standard, a four-point calibration was used with international reference materials and in-house standards (Spangenberg and Zufferey, 2019). The used standards included UNIL-Glycine ($\delta^{13}C$ = –26.10 ± 0.05‰), UNIL-Urea-1 ($\delta^{13}C$ = –43.00 ± 0.04‰), UNIL-Pyridine ($\delta^{13}C$ = –29.25 ± 0.06‰), and the RM USGS24 graphite ($\delta^{13}C$ = –16.05 ± 0.04‰). Analyses were done in duplicates. The accuracy of the analyses was checked periodically through the analysis of international RM standards not used for calibration. The reproducibility and precision of the EA/IRMS $\delta^{13}C$ analyses were determined by the standard deviation of separately replicated analyses and were better than 0.1‰.

3.5.2. Lithium isotopes

Sample digestion, column chemistry, and mass spectrometry were conducted in the London Geochemistry and Isotope Centre (LOGIC) laboratories at University College London (UCL) and Birkbeck, University of London. Clay samples were subjected to bulk digestion using concentrated HF, HNO_3, and $HClO_4$ in Teflon beakers on a hot plate at 130 °C, followed by steps in concentrated HNO_3 and 6 M HCl. The carbonate nodules were subject to leaching to separate the carbonate and detrital fractions. The carbonate fraction was extracted by leaching ~100 mg of sample in 8 ml 0.1 M HCl for 1 h (Pogge von Strandmann et al., 2013; Wilson et al., 2021), allowing a maximum of ~40 mg of calcium carbonate to be dissolved.

A standard method of elution was applied for lithium isotope separation in 0.2 M HCl. Two-column passes were applied through AG50W-X12 resin to ensure matrix removal (Pogge von Strandmann et al., 2013). Given that lithium isotopes are fractionated during ion chromatography, sample splits were collected before and after the lithium collection interval to assess column yields. For example, a 1% loss in yield at UCL has been assessed to lead to an offset of 1.7‰ (Wilson et al., 2021). Here, yields between two column passes were 99.8-100%, indicating excellent recovery.

Lithium isotope measurements were performed on a Nu Plasma 3 MC-ICP-MS at UCL, using a Cetac Aridus 2 desolvation system, 'super-lithium' cones, and standard-sample bracketing with the IRMM-016 Li standard (Pogge von Strandmann et al., 2019). Samples were measured at least three times within an analytical session, with each measurement integrating ~50 s, and the reported values are the mean and standard deviation (2sd) of these values, given in permil (‰) relative to the IRMM-016 standard. Accuracy and external reproducibility were assessed using seawater and USGS standard BCR-2, which gave δ^7Li values of +31.3 ± 0.6‰ (2sd, n = 28) and +2.5 ± 0.3‰ (n = 5), respectively.

3.5.3. Neodymium isotopes and rare earth element concentrations

After decarbonation using 10% HCl for 30 min, clays were separated from decarbonated sediments into <0.5 μm and 0.5-2 μm fractions (analytical protocol for size fraction separation reported in Jaimes-Gutierrez et al., 2024). A total of 18 samples (8 in the <0.5 μm size fraction and 10 in the 0.5-2 μm size fraction) were analysed for their neodymium (Nd) isotopic composition and their Nd and samarium (Sm) concentrations. Aliquots of about 1.5 mg of each clay fraction followed a sequential leaching procedure to remove Fe-Mn oxides and organic matter, based on the protocol of Bayon et al. (2002) and Gutjahr et al. (2007), slightly adapted. The Fe-Mn oxides were removed using a solution of 0.5 M hydroxylamine hydrochloride in 20% v/v acetic acid for 48h. Then, the organic matter was removed with a 5% H_2O_2 solution for 48h.

The leached samples were dried and digested by alkaline fusion following the protocol of Bayon et al. (2009), along with certified standards (BHVO-2, BRC-2) from the United States Geological Survey (USGS). Approximately 50 mg of each sample underwent alkaline fusion in a carbon crucible with 0.6 g of NaOH and 1.2 g of Na_2O_2 heated at 650°C for 12 min in a furnace, before adding ultrapure water in which Fe-hydroxides precipitated, concentrating rare earth elements. After centrifugation, the samples were dissolved in 3 ml 4 M HCl.

From this solution, an aliquot of 0.3 ml was extracted for analyses of Nd and Sm concentrations. Part of the samples were measured for their Nd and Sm concentrations on an Agilent 7500 quadrupole ICP-MS spectrometer in the Laboratoire Magmas et Volcans (LMV) in Clermont-Ferrand (France), and quantified using standard bracketing with a solution of BHVO-2 during the session. Accuracy and reproducibility were assessed using two BHVO-2 and one BCR-2 samples among the samples. Deviations of Nd and Sm concentrations from these standards were below 11%. The other part of the samples was measured for their Nd and Sm concentrations on a Thermo Scientific X-Series II® at the Pole Spectrométrie Océan in Brest (France), and quantified using multi-element calibration standards prepared from single element standards purchased from SCP science (Baie d'Urfé, Québec, Canada). Accuracy and reproducibility were assessed using one BHVO-2 and one BCR-2 sample, which were analysed among the samples. Deviations of Nd and Sm concentrations from these standards were below 7 %.

Purified neodymium fractions were isolated from the mother solution by ion chromatography following the protocol described in Gaitan et al. (2023) for the low-pressure, automated column chromatography PrepFAST-MC® system device, using AG50W-X8 (200-400 mesh) resin for rare earth element separation and Ln Spec (50-100 μm) resin for Nd separation. Part of the neodymium isotopic measurements was performed on a MC-ICP-MS Neptune Plus (Thermo Scientific) at the Laboratoire Magmas et Volcans in Clermont-Ferrand (France). Ratios were corrected for mass bias using an exponential law and a $^{143}Nd/^{144}Nd$ ratio of 0.7219. Mass-bias-corrected $^{143}Nd/^{144}Nd$ were normalised to a JNdi-1 value of 0.512115 (Tanaka et al., 2000). Repeated measurements of JNdi-1 throughout the session gave an external reproducibility of ± 0.000009 (2σ, n = 15), corresponding to ± 0.18 in the standard $\varepsilon_{Nd}(0)$ notation. Analyses of two BHVO-2 reference materials yielded a $^{143}Nd/^{144}Nd$ ratio of 0.512991±0.000005 for each, in excellent agreement with the published value of 0.512990±0.000010 (Weis et al., 2005). The other part of the samples was analysed on an MC-ICP-MS Neptune Plus (Thermo Scientific) at the ENS of Lyon (France). Ratios were corrected for mass bias using an exponential law and a $^{143}Nd/^{144}Nd$ ratio of 0.7219. Mass-bias-corrected $^{143}Nd/^{144}Nd$ values were normalised to a JNdi-1 value of 0.512115 (Tanaka et al., 2000). Repeated measurements of JNdi-1 throughout the session gave an external reproducibility of ± 0.000018 (2σ, n = 16), corresponding to ± 0.34 in the standard $\varepsilon_{Nd}(0)$ notation. Analyses of four BHVO-2 reference materials gave an average $^{143}Nd/^{144}Nd$ ratio of 0.512985 ± 0.000009 for each, in agreement with the published value of 0.512990 ± 0.000010 (Weis et al., 2006).

The data are reported in the standard epsilon notation $\varepsilon_{Nd} = [((^{143}Nd/^{144}Nd)_{sample}/(^{143}Nd/^{144}Nd)_{CHUR}) - 1] * 10^4)$, corrected for the radioactive decay of ^{147}Sm to ^{143}Nd based on the Nd and Sm concentrations measured for each sample ($^{147}Sm/^{144}Nd = Sm/Nd * 0.6049$), an age of 55.8 Ma, and the ^{147}Sm radioactive decay constant λ (6.54×10^{-12} y^{-1}; Lugmair & Marti, 1977). The CHUR (CHondritic Uniform Reservoir) $^{143}Nd/^{144}Nd$ ratio was also corrected using a $^{147}Sm/^{144}Nd$ ratio of 0.1960 and a present-day value of 0.512630 (Bouvier et al., 2008).

4. Results

4.1. Clay mineralogy in the Rin section

The clay mineralogy in the Rin section **(Fig. 5D, Table S1)** comprises mixed-layer illite-smectite (I/S), with a mean abundance of 34 ± 11 (1σ) wt.%; illite, 29 ± 9 wt.%; kaolinite, 30 ± 11 wt.%; and minor chlorite, 7 ± 5 wt.%. The pre-PETM samples have a mixed-layer I/S abundance of 42 ± 10 wt.%, decreasing to 32 ± 10 wt.%

during the body of the PETM. The kaolinite abundance increases from 22 ± 14 wt.% to 32 ± 9 wt.% during the
PETM body, while the illite and chlorite abundances remain stable.

4.2.   Organic matter carbon isotopes in the Rin section

Throughout the section, the mean $\delta^{13}C_{OM}$ value is -25.7‰, with a standard deviation (1σ) of 1.2‰ **(Fig. 5A, Table S2)**. The pre-PETM samples, between 5.8 and 9.4 m, have a mean value of -23.5 ± 0.5‰. A negative excursion begins in samples at 10.7 and 11.4 m, with values decreasing to -24.6 ± 0.1‰. The most depleted values occur between 12.8 and 38.9 m, with a mean of -26.3 ± 0.5‰. The final sample at 39.5 m, below the Alveolina Limestone, suggests a return to pre-PETM levels, with a value of -23.7‰.
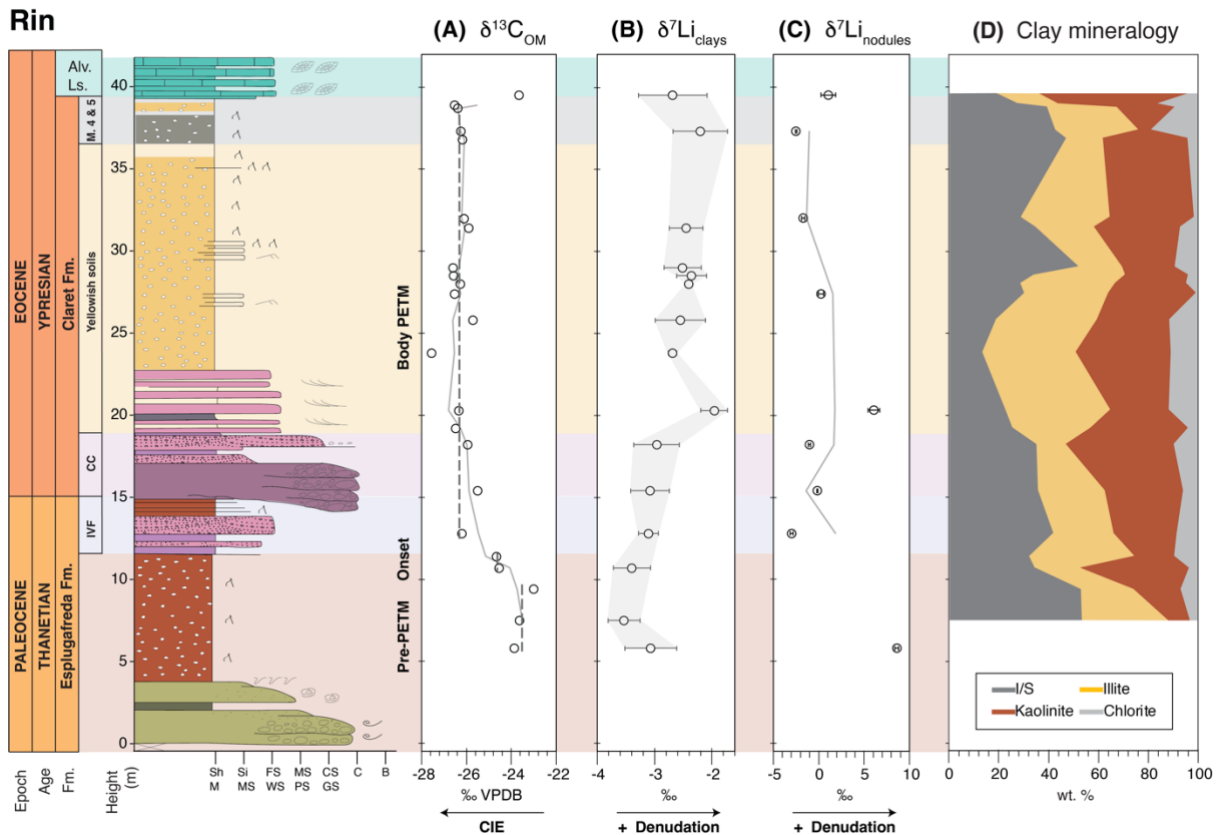
Figure 5. *Rin section isotopes and clay mineralogy. (A) The $\delta^{13}C_{OM}$ record shows the negative Carbon Isotope Excursion (CIE), with an onset before the Claret Conglomerate and sustained negative values until the Alveolina Limestone. (B) The CIE was accompanied by a positive excursion in lithium isotopes of the clays (δ^7Li_{clays}), reaching a 0.9‰ excursion in the Yellowish soils member. (C) Lithium isotopes in the carbonate nodules showed high variability and a less conclusive trend. (D) Rin section clay mineralogy. The pre-PETM and body intervals were determined based on the $\delta^{13}C_{OM}$ record and the stratigraphy. Dashed lines in panel A represent average values for $\delta^{13}C_{OM}$ in the pre-PETM and syn-PETM intervals. Grey bars in panel B outline the analytical uncertainty (2sd) of δ^7Li_{clays}.*

4.3.   Lithium isotopes in the Rin and Esplugafreda sections

The clays of the Rin section have a mean lithium isotope composition of -2.9 ± 0.5‰ (1σ) **(Fig. 5B, Table S2)**. Between 5.8 and 18.2 m, the mean composition is -3.4 ± 0.2‰. Above this, from 20.3 to 39.5 m, the mean composition is -2.6 ± 0.2‰, which corresponds to a shift towards more positive values of ~0.8‰. The minimum value of -3.7‰ is seen before the Claret Conglomerate, and the maximum value of -2.2‰ occurs immediately after the Claret Conglomerate, indicating a total range of up to ~1.5‰. The δ^7Li values measured on carbonate nodules have a maximum value of 8.6‰, a minimum value of -3.0‰, and a mean composition of 0.9 ± 4.0‰ **(Fig. 5C)**. No clear temporal trend is observed in the $\delta^7Li_{nodules}$ record. No systematic correlation is observed between δ^7Li_{clays} and the relative abundance of individual clay minerals within analytical uncertainty (Fig. S1).

At the Esplugafreda section, the clays have a mean lithium isotope composition of -3.7 ± 0.7‰ **(Fig. 6B, Table S3)**. The pre-PETM samples (0-10 m and 21-28 m, Jaimes-Gutierrez et al., 2024 and references therein) have a

mean composition of -3.8 ± 0.2‰. The POE samples (~15–21 m) have a composition of -3.2 ± 0.2‰, and the syn-PETM sediments have a composition of -3.0 ± 0.2‰, indicating a PETM shift towards more positive values of ~0.8‰. The post-PETM sediments have a composition of -4.5 ± 0.4‰. Samples from the pre-PETM, Pre-Onset Excursion (POE), and syn-PETM intervals display relatively heavier δ⁷Li$_{clays}$ values, whereas recovery-phase samples form a distinct cluster characterised by lighter δ⁷Li$_{clays}$ (Fig. S2).

4.4. Neodymium isotopes in the Esplugafreda sections

Throughout the Esplugafreda section, the 0.5–2 µm clays have a mean ε$_{Nd}$ (t = 55.8 Ma) composition of -10.94 ± 0.16 (2σ), while the <0.5 µm fraction has a mean composition of -10.88 ± 0.11 (**Fig. 6C, Table S4**). In comparison, the typical analytical uncertainty on any individual sample measurement was 0.21 (2σ). Hence, these values are considered constant through time, with no deviation significantly outside the analytical uncertainty. The neodymium isotope measurements on the <0.5 µm fraction are also indistinguishable from those on the 0.5-2 µm fraction (**Fig. 6C**).
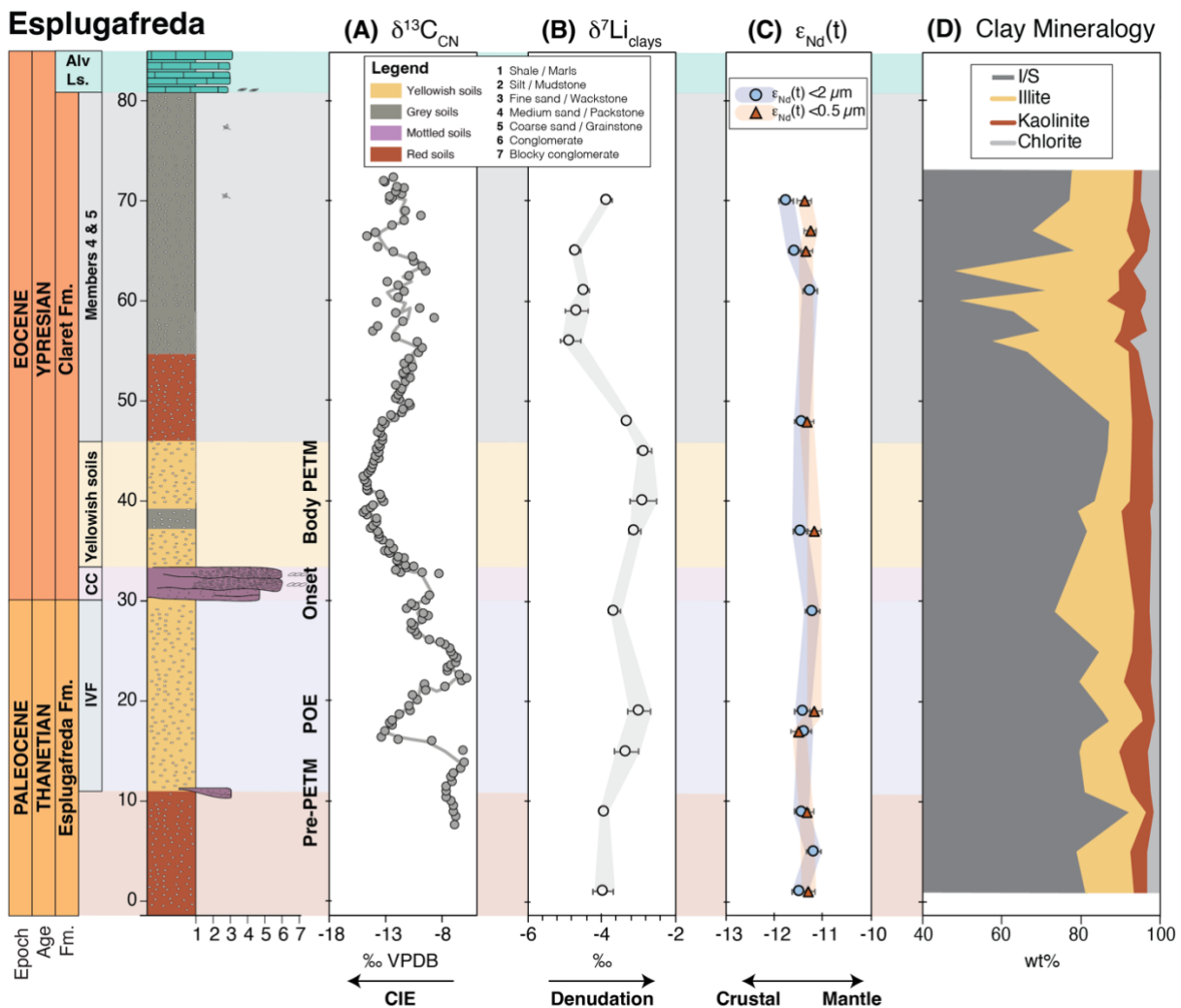
Figure 6. *Esplugafreda section isotopes and clay mineralogy. (A) The δ¹³C record from microcrystalline carbonate nodules (from Khozyem, 2013) shows a negative carbon isotope excursion during the Pre-Onset Excursion (POE) and during the main body of the PETM. (B) Positive excursions in lithium isotopes of the clays (δ⁷Li$_{clays}$) during both the POE and the main CIE of the PETM. (C) Neodymium isotopes (ε$_{Nd}$ (t = 55.8 Ma)) show no variation throughout the section, indicating constant provenance. (D) Esplugafreda section clay mineralogy (modified from Jaimes-Gutierrez et al., 2024).*

5. Discussion

5.1. The PETM in the Rin section

The PETM sediments in the Rin section represent an archive of the climatic perturbation in a coastal terrestrial setting (Pujalte et al., 2014; Prieur et al., 2025). This locality records a negative δ¹³C$_{OM}$ excursion of -2.8‰ from

11

pre- to syn-PETM (**Fig. 5**), in agreement with the CIE excursion of 3-5 ‰ identified in other southern Pyrenean sections and other global settings (e.g. Schmitz et al., 2001; Schmitz and Pujalte, 2007; McInerney and Wing, 2011; Pujalte et al., 2015). The slightly reduced magnitude compared to the global record is consistent with observed systematic differences in the CIE across different types of terrestrial archives, with paleosol carbonates typically recording a 1-2 ‰ larger CIE than paleosol organic matter (Bowen et al., 2004; Cotton et al., 2015; Gallagher et al., 2019). We do not identify the POE in the Rin section, and we suggest that it may have been missed due to its occurrence further down in the section. Likewise, the recovery to pre-PETM values is also largely absent, with just one sample below the Alevolina Limestone showing less depleted $\delta^{13}C_{OM}$ values.

The five members recognised in the Claret Fm. show an evolution from the eastern terrestrial setting into the western marine domain. At Esplugafreda (**Fig. 6**), the five members are recorded (Basilici et al., 2022 and references therein), including Member 1, IVF (pre-PETM); Member 2, the Claret Conglomerate (Onset at Esplugafreda); Member 3, Yellowish soils (syn-PETM, or body of the PETM); Member 4, red paleosols with gypsum; and Member 5, consisting of red mudstones with carbonate nodules (e.g. Schmitz and Pujalte, 2007; Baceta et al., 2011; Pujalte et al., 2014; Colombera et al., 2017; Basilici et al., 2022). However, Member 4, the gypsum-rich member, only occurs in the eastern part of the basin (Pujalte et al., 2014). Given the coastal position of the Rin section, at the marine-continental transition and only ~20 km east of the Serraduy section, representing the westernmost expression of the interfingering between continental deposits from the Esplugafreda Fm. and marine carbonates (Prieur et al., 2025), the absence of Member 4 supports a further downstream position of the Rin section relative to the Esplugafreda floodplain section.

Duller et al. (2019) estimated a lag time of approximately 16.5 ± 7.5 kyr between the CIE and the onset of coarse-grained deposition at terrestrial sites in the Pyrenees. While sections such as Tendrui, Claret, and Campo (Pujalte et al., 2009; Domingo et al., 2009) display a stratigraphic offset consistent with this lag, the Esplugafreda section does not show such an offset (Duller et al., 2019). In the Rin section discussed here, we observe a clear offset between the onset of the CIE and the arrival of the Claret Conglomerate (**Fig. 5**). To correctly position the lag time and explore the missing POE, future work could focus on high-resolution $\delta^{13}C$ characterisation of the section.

The clay mineralogy at Rin further suggests a potential signal propagation effect. A shift from smectite-dominated clays during the pre-PETM interval to an increase in kaolinite during the syn-PETM interval (**Fig. 5D**) could indicate a transition to more hydrolysing conditions and to an increase in weathering intensity, or enhanced erosion of former sedimentary formations rich in kaolinite. However, this trend also corresponds to a downstream transition from authigenic smectite-rich paleosols at Esplugafreda (**Fig. 6D**) (e.g. Khozyem, 2013; Basilici et al., 2022; Jaimes-Gutierrez et al., 2024) to kaolinite-dominated sediments in the Zumaia deep-marine section (Gawenda et al., 1999; Schmitz et al., 2001; Bolle and Adatte, 2001). This mineralogical gradient from Esplugafreda to Rin and Zumaia underscores the system connectivity across the basin (Pujalte et al., 2014). However, such variations in clay composition may also reflect differences in sediment provenance (although temporal changes are not observed in the ϵ_{Nd} record from Esplugafreda); differential mineral transport; enhanced floodplain weathering; an increased proportion of eroded sedimentary formations downstream, bringing reworked kaolinite (Pujalte et al., 2015); or a larger catchment area feeding the marine system (Chamley, 1989 and references therein).

An influence from Marine Authigenic Aluminosilicate Clay (MAAC) formation is feasible in the coastal setting of the Rin section, but is unlikely to have been a significant driver of changes in the lithium isotope record given the dominance of continental inputs. In marine sediments, clay mineral assemblages dominated by kaolinite, illite, smectite, and mixed-layer illite/smectite are generally interpreted as mainly detrital in origin, reflecting continental weathering and fluvial transport rather than in situ marine precipitation (Thiry, 2000; Fagel, 2007; Velde and Meunier, 2008). Although the authigenic formation of these clay minerals is known to occur in marine environments, it is typically restricted to specific conditions or processes, such as the alteration of volcanic ash, or evaporitic or hydrothermal settings, and is therefore not expected to be significant in shallow, nearshore depositional systems with high terrigenous sedimentation rates (Środoń, 2001; Wise et al., 2001; Meunier, 2005). In contrast to glauconite or other green clays, which may form authigenically under low sedimentation rates, kaolinite and illite in coastal marine settings are widely regarded as inherited from continental sources (Thiry, 2000; Meunier, 2005; Fagel, 2007; Presti and Michalopoulos, 2008; Bernhardt et al., 2020). Given the dominantly continental depositional setting of the Rin section and the large detrital clay input inferred for the nearshore environment, any MAAC contribution is expected to have been minor relative to the terrigenous signal. MAAC form from isotopically heavy seawater or porewaters and are therefore expected to have δ^7Li values substantially higher than detrital clays (Pogge von Strandmann et al., 2021a). A simple mass balance indicates than even under extreme assumptions (i.e. 2 wt.% MAAC, 10‰ δ^7Li values), such a contribution would shift bulk values by <0.3‰, far smaller than the observed PETM excursion.

5.2. Evolution of weathering intensity in the continental realm of the Southern Pyrenees

Our $\delta^7 Li_{clays}$ records from Rin and Esplugafreda both show a positive (~1‰) lithium isotope excursion in the continental Southern Pyrenees during the onset and body of the PETM (**Fig. 7**). The $\delta^7 Li$ values from carbonate nodules at Rin show greater variability (**Fig. 5C**), but remain inconclusive due to potential clay contamination or cation exchange between clays and carbonates (e.g. Pogge von Strandmann et al., 2019). Given the high Li content in silicate minerals, even a minor clay particle content in the nodules could contaminate the carbonate signature. Critically, the invariant ϵ_{Nd} composition of both size fractions throughout the Esplugafreda record (**Fig. 6C**) supports a constant provenance of the sediments, which suggests that the $\delta^7 Li_{clays}$ records can be reliably interpreted as a reflection of weathering regime changes in response to the climatic perturbation.
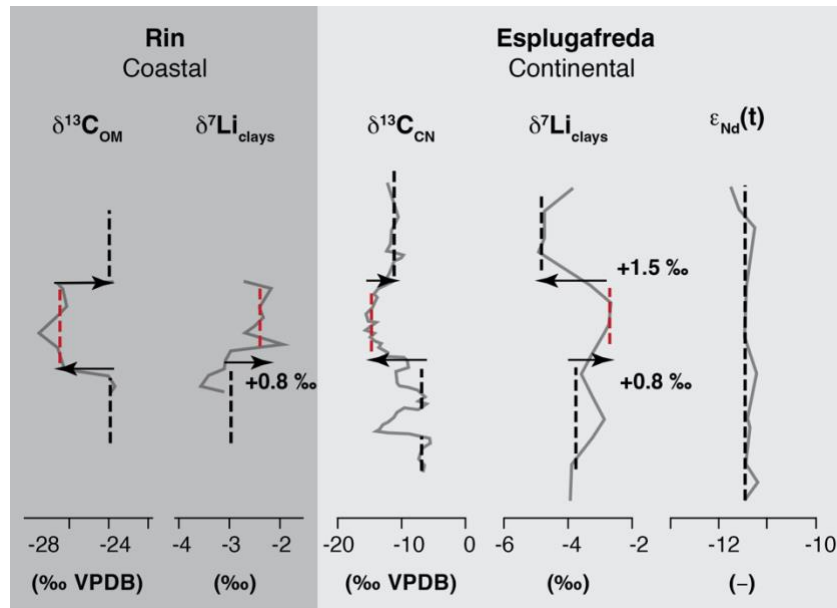

Figure 7. Comparison of isotopic results from the Rin and Esplugafreda sections. Grey solid lines show the raw data, while dashed black and red lines indicate typical values for different intervals, where red represents the PETM. The pre-PETM and post-PETM shifts are indicated with the black arrows, and the magnitudes of the $\delta^7 Li_{clays}$ excursions are reported.

In many other PETM records, both marine and terrestrial $\delta^7 Li$ values show a negative excursion from pre-PETM to syn-PETM conditions. Pogge von Strandmann et al. (2021) documented a negative $\delta^7 Li$ excursion of ~3‰ during the PETM in several marine carbonate sections and in detrital shales, indicating intensified global erosion rates (by 2–3×) and a 50–60% increase in silicate weathering fluxes, which was proposed to have contributed to climate stabilisation. Ramos et al. (2022) also found a negative $\delta^7 Li_{clays}$ excursion, albeit with a smaller magnitude of ~1.5‰, in fine sediments of the Bighorn Basin, North America during the PETM, and this change was sustained during the recovery phase. Consistent with these results, Chen et al. (2023) found a negative $\delta^7 Li_{clays}$ excursion of ~3‰ in the Nanyang Basin, East Asia, which, together with the negative $\delta^7 Li$ excursion in the lacustrine carbonates, was interpreted as recording a doubling of the regional silicate weathering intensity during the PETM.

Why, then, do the Southern Pyrenees floodplains record a positive $\delta^7 Li_{clays}$ excursion during the PETM? We interpret the positive $\delta^7 Li_{clays}$ excursion during the PETM as a shift towards increased incongruent weathering (moderate weathering regime), characterised by enhanced clay formation in the floodplain deposits. This regime would be characterised by increased chemical weathering, but relatively greater increases in physical erosion and sediment transport (e.g. Pujalte et al., 2015; Chen et al., 2018; Prieur et al., 2024), due to enhanced runoff causing short water residence times and rapid sediment export (i.e. lower *W/D*; **Fig. 8**). Hydrological changes during the PETM are widely documented in the Southern Pyrenees (Schmitz and Pujalte, 2007; Pujalte et al., 2015; Chen et al., 2018; Rush et al., 2021; Prieur et al., 2024, 2025; Jaimes-Gutierrez et al., 2024) and likely played a central role in driving those weathering changes. A shift towards more intense, episodic rainfall, without an increase in mean annual precipitation (Rush et al., 2021), could have reduced infiltration, increased runoff, and shortened water–mineral interaction times. These processes would lead to decreased clay formation in the uplands by

529 shortening water-rock interaction times (Kump et al., 2000; Riebe et al., 2004), while shifting clay production and
530 accumulation towards lowland environments, where longer sediment residence times promote authigenic clay
531 formation, consistent with modern river floodplain processes (e.g. Dellinger et al., 2015; Maffre et al., 2020). We
532 also note that weathering processes are highly heterogeneous, and therefore global variability during the PETM
533 can be expected (e.g. Frings, 2019). Critically, A decrease in *W/D* can lead both to positive or negative δ^7Li
534 excursions, depending on the starting weathering regime (Krause et al., 2023).
535
536 Increasing evaporation, as recorded by gypsum lenses in Esplugafreda (Baceta et al., 2011; Khozyem, 2013;
537 Jaimes-Gutierrez et al., 2024 and references therein), could also result in oversaturated pore waters, favouring
538 clay formation. Experimental and field-based studies show that enhanced evaporation and reduced water
539 availability increase the dissolved δ^7Li values in soil and pore waters, leading to higher δ^7Li compositions of clays
540 forming in equilibrium with these fluids (Xu et al., 2022; Pogge von Strandmann et al., 2023). Hydrological
541 controls can also influence the δ^7Li$_{clays}$ signatures by regulating water-rock interactions, sediment transport, and
542 secondary mineral formation **(Fig. 8)**. In supply-limited weathering regimes, increased runoff shortens water–
543 rock interaction times and lowers dissolved δ^7Li values in river waters (Zhang et al., 2022), while enhanced
544 sediment transfer promotes sediment storage and prolonged water–sediment interaction in floodplains, where
545 continued clay alteration and isotopic re-equilibration can yield relatively higher δ^7Li values in the clay fraction
546 preserved in lowland deposits. Overall, rapid sediment transport limits basin-scale weathering intensity, despite
547 localised clay formation in floodplain environments.
548
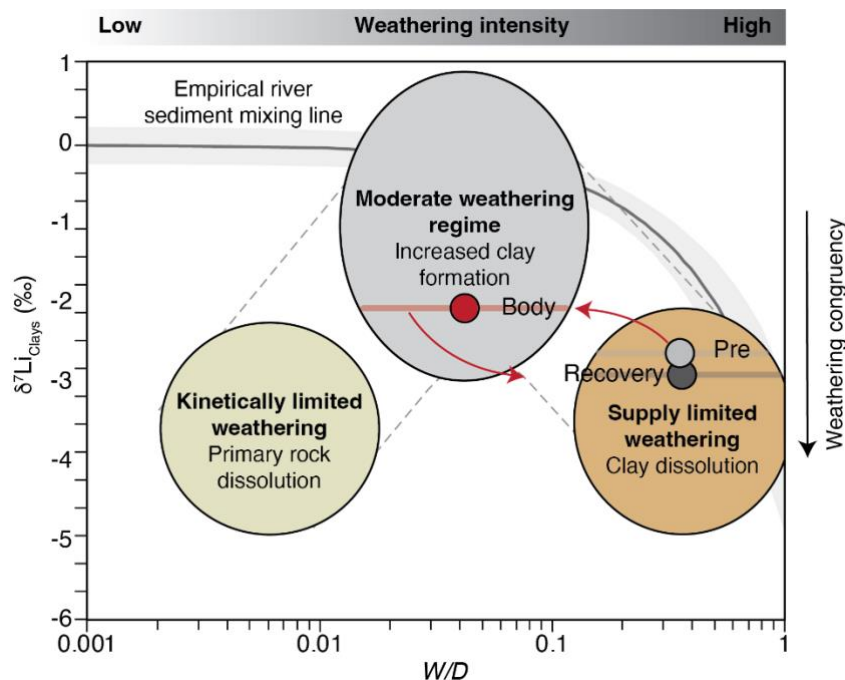
549
550 ***Figure 8.*** *Weathering regime change from pre-PETM to syn-PETM based on δ^7Li$_{clays}$ in the continental deposits*
551 *of the Southern Pyrenees. The floodplain records were characterised by a decrease in weathering intensity and*
552 *an increase in clay formation. Enhanced transport efficiency resulted in a major increase in physical erosion,*
553 *with reaction kinetics limiting chemical weathering. Modified from Dellinger et al. (2015, 2017). At low W/D, the*
554 *empirical river sediment mixing line includes the effects of mixing with primary minerals.*

555 In the Esplugafreda section, the Recovery phase sees a shift towards more negative values than the pre-PETM
556 conditions. During this interval, we observe a coeval increase in illite, kaolinite, and chlorite abundances in the
557 Esplugafreda section (Jaimes-Gutierrez et al., 2024). This shift in the clay mineral assemblage strongly suggests
558 an increase in detrital input. For this reason, we consider that the observed excursion cannot be straightforwardly
559 interpreted as a change in weathering intensity, but rather reflect the clay mineral assemblage (Fig. S2).
560
561 Temperature effects on lithium isotope fractionation are minor in the Southern Pyrenees. While lithium isotope
562 fractionation during clay formation is temperature-dependent (Vigier et al., 2008; Li and West, 2014), the
563 fractionation factor (α) for incorporation in smectite is nearly constant across typical surface weathering
564 temperatures (Vigier et al., 2008). Using the ~3 ºC warming estimated for the continental Pyrenees across the
565 PETM (Jaimes-Gutierrez et al., 2024), the maximum temperature-driven change in clay δ^7Li values is expected
566 to be only a few tenths of a per mil (Li and West, 2014). This effect would shift clay δ^7Li values slightly towards

567 heavier values and could therefore contribute marginally to the observed excursion, but it is insufficient to explain
568 the full magnitude of the ~1‰ positive δ^7Li_{clays} shift observed in the records. Hence, climatic and hydrological
569 processes, rather than direct temperature effects, must dominate the δ^7Li signal.

571 The differences in δ^7Li values between river water and bedrock are controlled by the balance between lithium
572 release by mineral dissolution and lithium removal by secondary mineral formation (Bouchez et al., 2013). The
573 Southern Pyrenees during the PETM was a relatively high-erosion regime, such that physical erosion dominated,
574 increasing the sediment supply and exposing fresh minerals (Schmitz and Pujalte, 2007; Pujalte et al., 2015, 2016;
575 Chen et al., 2018; Prieur et al., 2024, 2025). When erosion exposes fresh minerals, weathering rates increase with
576 total denudation, albeit less strongly than the increases in erosion, consistent with shared controls on chemical
577 weathering and physical denudation rates (Riebe et al., 2004; West et al., 2005). Even though high-relief regions
578 produce weakly weathered sediments, their high sediment yields and moderate clay formation rates result in
579 elevated weathering fluxes (Gaillardet et al., 1999). Therefore, we propose that the Southern Pyrenean floodplains
580 record a shift from a high-weathering intensity regime to a moderate-weathering intensity regime during the
581 PETM (**Fig. 8**). The pre-PETM conditions were characterised by a low reactivity of the parent lithology (Kump
582 and Arthur, 1997; Caves Rugenstein et al., 2019), associated with the carbonate-rich, reworked sediments in the
583 floodplain deposits, and hence low total weathering fluxes. The above scenario is also consistent with the "system-
584 clearing" event documented in western North America (Foreman et al., 2012), where sediment transport surged
585 in response to rapid climatic forcing, as well as with other Eocene warming events such as the Mid-Eocene
586 Climatic Optimum, which saw a shift towards enhanced clay formation and a lower weathering intensity (Krause
587 et al., 2023).

589 The progressive increase in kaolinite content from Esplugafreda to Rin may reflect an evolving weathering signal
590 during sediment transport from the hinterland towards the coastal plains, which potentially extended into the
591 marine realm. This scenario supports a basin-wide connectivity between climate-driven terrestrial processes and
592 marine sedimentary records. In addition, the increase in kaolinite content from Esplugafreda to Rin supports a
593 shift in clay formation processes during the PETM. Kaolinite is typically associated with intense leaching and
594 more advanced weathering, often forming under warm, humid, and periodically saturated conditions (Chamley,
595 1989; Velde and Meunier, 2008). Hence, its enrichment suggests either intensified in-situ clay formation in the
596 floodplains or increased transport of weathered material from the uplands to the lowlands. In either case, this shift
597 implies greater clay mineral production, consistent with a more incongruent weathering regime driving the
598 observed positive δ^7Li_{clays} excursion. Alternatively, enhanced kaolinite supply from the erosion-driven
599 exhumation of older sediments cannot be ruled out based on the current evidence.

601 Despite these insights, key questions remain unresolved. In particular, a comprehensive study of the provenance
602 and evolution of clay mineralogy is still needed to determine to what extent the observed patterns along the
603 sediment routing system reflect changes in weathering intensity, differential mineral transport, or sediment
604 reworking. Equally important is the need to constrain the precise age of the clay formation in relation to the timing
605 of the different phases of the PETM, which is critical for reconstructing the temporal dynamics of the weathering
606 regime in the Southern Pyrenees. Addressing these gaps will be crucial for better understanding how continental
607 weathering systems responded to extreme climatic perturbations in the past and how they may behave under future
608 global warming scenarios.

610 **6.   Conclusions**

611 We explored the silicate weathering response to the PETM in two terrestrial sections from the Tremp-Graus Basin
612 of the Southern Pyrenees. These floodplain records show a positive δ^7Li_{clays} excursion, contrasting with the
613 commonly observed global negative δ^7Li excursion in clays and carbonates. We interpret this excursion as
614 reflecting a shift towards a moderate-intensity, incongruent weathering regime from an initial high-intensity,
615 supply-limited regime. The high erosion rates associated with increased extreme rainfall events and channel
616 mobility may have been the central factor influencing sediment residence times, with rapid sediment transport
617 limiting the extent of chemical weathering. Nevertheless, the elevated denudation rates would have led to higher
618 sediment and dissolved cation fluxes to the ocean, thereby enhancing regional CO_2 drawdown.

620 We explored two potential archives for recording continental weathering processes using lithium isotopes. The
621 clay records show a distinct response, reflected in positive δ^7Li_{clays} excursions synchronous with the negative CIE.
622 However, the $\delta^7Li_{nodules}$ signal recorded in the carbonate nodules is less conclusive, and we interpret the high
623 temporal variability as a sign of potential contamination by clays in the nodules. Given that Li concentrations in
624 silicate minerals are higher than in carbonates by several orders of magnitude, even minor amounts of clays could

have resulted in a mixed response in the nodules. Future studies should explore weaker leaching approaches on such nodules and seek to validate such data with major and trace element analyses.

Provided coeval formation, the increase in kaolinite content from Esplugafreda to Rin provides mineralogical support for more hydrolysing conditions and clay formation during the PETM in the Tremp-Graus Basin, reinforcing the interpretation of more incongruent weathering under altered hydroclimatic conditions. Notably, the parent material in these floodplain paleosols is carbonate-rich and relatively unreactive. These results highlight the critical role of hydrological controls, especially rainfall intensity, runoff dynamics, and sediment residence time, in shaping continental weathering responses during extreme climate events.

Finally, we propose that to fully quantify weathering dynamics during the PETM in the Southern Pyrenees, further work is needed to: (1) constrain the chronology of clay formation; (2) trace the evolution of clay mineralogy and provenance from source to sink; and (3) integrate continental and marine weathering records across the sediment routing system. Together, these steps will be essential for refining our understanding of weathering behaviour and the associated climate feedbacks under rapid climatic perturbations, and for improving predictions of Earth's surface processes in semi-arid floodplain systems in future global warming scenarios.

Acknowledgments

Author contributions

R.J.G. performed sample collection, analytical work (clay mineralogy, RockEval, lithium and neodymium ion-exchange chromatography), data interpretation, visualisation, and original manuscript writing.
M.P. contributed to sample collection, data interpretation, visualisation, and manuscript writing.
D.J.W. and P.A.E.P.V.S. contributed to analytical work on lithium isotopes, data interpretation, and manuscript writing.
E.P. conducted analytical work on neodymium isotopes, data interpretation, and manuscript writing.
T.A. conducted RockEval analyses, contributed to data interpretation, and manuscript writing.
J.E.S. conducted $\delta^{13}C$ analyses on organic matter and contributed to data interpretation and manuscript writing.
S.C. acquired funding for the project, contributed to sample collection, data interpretation, and manuscript writing.

Conflict of interest
The authors declare that they have no conflict of interest relevant to this study.

References

Adatte, T., Stinnesbeck, W., and Keller, G., 1996, Lithostratigraphic and mineralogic correlations of near K/T boundary clastic sediments in northeastern Mexico: Implications for origin and nature of deposition, *in* The Cretaceous-Tertiary Event and Other Catastrophes in Earth History, Geological Society of America, doi:10.1130/0-8137-2307-8.211.

Anderson, S.P., Von Blanckenburg, F., and White, A.F., 2007, Physical and Chemical Controls on the Critical Zone: Elements, v. 3, p. 315–319, doi:10.2113/gselements.3.5.315.

Baceta, J.I., Pujalte, V., and Bernaola, G., 2005, Paleocene coralgal reefs of the western Pyrenean basin, northern Spain: New evidence supporting an earliest Paleogene recovery of reefal ecosystems: Palaeogeography, Palaeoclimatology, Palaeoecology, v. 224, p. 117–143, doi:10.1016/j.palaeo.2005.03.033.

Baceta, J.I., Pujalte, V., Wright, V.P., and Schmitz, B., 2011, Carbonate platform models, sea/ level changes and extreme climatic events during the Paleocene/ Eocene greenhouse interval: A basin-platform-coastal plain transect across the southern Pyrenean basin: 28th IAS Meeting of Sedimentology.

677 Barefoot, E.A., Nittrouer, J.A., Foreman, B.Z., Hajek, E.A., Dickens, G.R., Baisden, T., and Toms, L., 2022,
678   Evidence for enhanced fluvial channel mobility and fine sediment export due to precipitation
679   seasonality during the Paleocene-Eocene thermal maximum: v. 50, p. 116–120, doi:10.1130/G49149.1.

680 Basilici, G., Colombera, L., Soares, M.V.T., Arévalo, O.J., Mountney, N.P., Lorenzoni, P., de Souza Filho,
681   C.R., Mesquita, Á.F., and Janočko, J., 2022, Variations from dry to aquic conditions in Vertisols
682   (Esplugafreda Formation, Eastern Pyrenees, Spain): Implications for late Paleocene climate change:
683   Palaeogeography, Palaeoclimatology, Palaeoecology, v. 595, p. 110972,
684   doi:10.1016/j.palaeo.2022.110972.

685 Bauer, K.K., Vennemann, T.W., and Gilg, H.A., 2016, Stable isotope composition of bentonites from the Swiss
686   and Bavarian Freshwater Molasse as a proxy for paleoprecipitation: Palaeogeography,
687   Palaeoclimatology, Palaeoecology, v. 455, p. 53–64, doi:10.1016/j.palaeo.2016.02.002.

688 Bayon, G., Burton, K.W., Soulet, G., Vigier, N., Dennielou, B., Etoubleau, J., Ponzevera, E., German, C.R., and
689   Nesbitt, R.W., 2009, Hf and Nd isotopes in marine sediments: Constraints on global silicate
690   weathering: Earth and Planetary Science Letters, v. 277, p. 318–326, doi:10.1016/j.epsl.2008.10.028.

691 Bayon, G., German, C.R., Boella, R.M., Milton, J.A., Taylor, R.N., and Nesbitt, R.W., 2002, An improved
692   method for extracting marine sediment fractions and its application to Sr and Nd isotopic analysis:
693   Chemical Geology, v. 187, p. 179–199, doi:10.1016/S0009-2541(01)00416-8.

694 Behar, F., Beaumont, V., and De B. Penteado, H.L., 2001, Rock-Eval 6 Technology: Performances and
695   Developments: Oil & Gas Science and Technology, v. 56, p. 111–134, doi:10.2516/ogst:2001013.

696 Bernhardt, A., Oelze, M., Bouchez, J., Von Blanckenburg, F., Mohtadi, M., Christl, M., and Wittmann, H.,
697   2020, ^{10}Be/^{9}Be Ratios Reveal Marine Authigenic Clay Formation: Geophysical Research Letters, v.
698   47, p. e2019GL086061, doi:10.1029/2019GL086061.

699 Bolle, M.-P., and Adatte, T., 2001, Palaeocene- early Eocene climatic evolution in the Tethyan realm: clay
700   mineral evidence: Clay Minerals, v. 36, p. 249–261, doi:10.1180/000985501750177979.

701 Bouchez, J., Von Blanckenburg, F., and Schuessler, J.A., 2013, Modeling novel stable isotope ratios in the
702   weathering zone: American Journal of Science, v. 313, p. 267–308, doi:10.2475/04.2013.01.

703 Bouvier, A., Vervoort, J.D., and Patchett, P.J., 2008, The Lu–Hf and Sm–Nd isotopic composition of CHUR:
704   Constraints from unequilibrated chondrites and implications for the bulk composition of terrestrial
705   planets: Earth and Planetary Science Letters, v. 273, p. 48–57, doi:10.1016/j.epsl.2008.06.010.

706 Bowen, G.J., Beerling, D.J., Koch, P.L., Zachos, J.C., and Quattlebaum, T., 2004, A humid climate state during
707   the Palaeocene/Eocene thermal maximum: Nature, v. 432, p. 495–499, doi:10.1038/nature03115.

708 Bufe, A., Hovius, N., Emberson, R., Rugenstein, J.K.C., Galy, A., Hassenruck-Gudipati, H.J., and Chang, J.-M.,
709   2021, Co-variation of silicate, carbonate and sulfide weathering drives CO2 release with erosion:
710   Nature Geoscience, v. 14, p. 211–216, doi:10.1038/s41561-021-00714-3.

711 Carmichael, M.J. et al., 2017, Hydrological and associated biogeochemical consequences of rapid global
712   warming during the Paleocene-Eocene Thermal Maximum: Global and Planetary Change, v. 157, p.
713   114–138, doi:10.1016/j.gloplacha.2017.07.014.

714 Caves, J.K., Jost, A.B., Lau, K.V., and Maher, K., 2016, Cenozoic carbon cycle imbalances and a variable
715   weathering feedback: Earth and Planetary Science Letters, v. 450, p. 152–163,
716   doi:10.1016/j.epsl.2016.06.035.

717 Caves Rugenstein, J.K., Ibarra, D.E., and von Blanckenburg, F., 2019, Neogene cooling driven by land surface
718   reactivity rather than increased weathering fluxes: Nature, v. 571, p. 99–102, doi:10.1038/s41586-019-
719   1332-y.

720 Chamley, H., 1989, Clay Sedimentology: Berlin, Heidelberg, Springer Berlin Heidelberg, doi:10.1007/978-3-
721   642-85916-8.

722 Chen, Z., Ding, Z., Yang, S., Sun, J., Zhu, M., Xiao, Y., Tong, F., and Liang, Y., 2023, Strong Coupling
723   Between Carbon Cycle, Climate, and Weathering During the Paleocene-Eocene Thermal Maximum:
724   Geophysical Research Letters, v. 50, p. e2023GL102897, doi:10.1029/2023GL102897.

725 Chen, C., Guerit, L., Foreman, B.Z., Hassenruck-Gudipati, H.J., Adatte, T., Honegger, L., Perret, M., Sluijs, A.,
726   and Castelltort, S., 2018, Estimating regional flood discharge during Palaeocene-Eocene global
727   warming: Scientific Reports, v. 8, p. 13391, doi:10.1038/s41598-018-31076-3.

728 Colombera, L., Arévalo, O.J., and Mountney, N.P., 2017, Fluvial-system response to climate change: The
729   Paleocene-Eocene Tremp Group, Pyrenees, Spain: Global and Planetary Change, v. 157, p. 1–17,
730   doi:10.1016/j.gloplacha.2017.08.011.

731 Cotton, J.M., Sheldon, N.D., Hren, M.T., and Gallagher, T.M., 2015, Positive feedback drives carbon release
732   from soils to atmosphere during Paleocene/Eocene warming: American Journal of Science, v. 315, p.
733   337–361, doi:10.2475/04.2015.03.

734 Dellinger, M., Bouchez, J., Gaillardet, J., Faure, L., and Moureau, J., 2017, Tracing weathering regimes using
735   the lithium isotope composition of detrital sediments: Geology, v. 45, p. 411–414,
736   doi:10.1130/G38671.1.

737 Dellinger, M., Gaillardet, J., Bouchez, J., Calmels, D., Louvat, P., Dosseto, A., Gorge, C., Alanoca, L., and
738   Maurice, L., 2015, Riverine Li isotope fractionation in the Amazon River basin controlled by the
739   weathering regimes: Geochimica et Cosmochimica Acta, v. 164, p. 71–93,
740   doi:10.1016/j.gca.2015.04.042.

741 Dessert, C., Dupré, B., Gaillardet, J., François, L.M., and Allègre, C.J., 2003, Basalt weathering laws and the
742   impact of basalt weathering on the global carbon cycle: Chemical Geology, v. 202, p. 257–273,
743   doi:10.1016/j.chemgeo.2002.10.001.

744 Dickens, G.R., O'Neil, J.R., Rea, D.K., and Owen, R.M., 1995, Dissociation of oceanic methane hydrate as a
745   cause of the carbon isotope excursion at the end of the Paleocene: Paleoceanography, v. 10, p. 965–
746   971, doi:10.1029/95PA02087.

747 Domingo, L., López-Martínez, N., Leng, M.J., and Grimes, S.T., 2009, The Paleocene–Eocene Thermal
748   Maximum record in the organic matter of the Claret and Tendruy continental sections (South-central
749   Pyrenees, Lleida, Spain): Earth and Planetary Science Letters, v. 281, p. 226–237,
750   doi:10.1016/j.epsl.2009.02.025.

751 Dreyer, T., 1993, Quantified Fluvial Architecture in Ephemeral Stream Deposits of the Esplugafreda Formation
752   (Palaeocene), Tremp-Graus Basin, Northern Spain, *in* Marzo, M. and Puigdefábregas, C. eds., Alluvial
753   Sedimentation, Wiley, p. 337–362, doi:10.1002/9781444303995.ch23.

754 Duller, R.A., Armitage, J.J., Manners, H.R., Grimes, S., and Jones, T.D., 2019, Delayed sedimentary response
755   to abrupt climate change at the Paleocene-Eocene boundary, northern Spain: Geology, v. 47, p. 159–
756   162, doi:10.1130/G45631.1.

757 Eichenseer, H., 1988, Facies Geology Of Late Maestrichtian To Early Eocene Coastal And Shallow Marine
758   Sediments (Tremp-Graus Basin, Northeastern Spain):

759 Eichenseer, H., and Luterbacher, H., 1992, The marine paleogene of the tremp region (NE Spain)-depositional
760   sequences, facies history, biostratigraphy and controlling factors: Facies, v. 27, p. 119–151,
761   doi:10.1007/BF02536808.

762 Espitalie, J., Deroo, G., and Marquis, F., 1985, La pyrolyse Rock-Eval et ses applications. Deuxième partie.:
763   Revue de l'Institut Français du Pétrole, v. 40, p. 755–784, doi:10.2516/ogst:1985045.

764 Fagel, N., 2007, Chapter Four Clay Minerals, Deep Circulation and Climate, *in* Developments in Marine
765   Geology, Elsevier, v. 1, p. 139–184, doi:10.1016/S1572-5480(07)01009-3.

766 Foreman, B.Z., Heller, P.L., and Clementz, M.T., 2012, Fluvial response to abrupt global warming at the
767   Palaeocene/Eocene boundary: Nature, v. 491, p. 92–95, doi:10.1038/nature11513.

768 Frings, P.J., 2019, Palaeoweathering: How Do Weathering Rates Vary with Climate? Elements, v. 15, p. 259–
769   265, doi:10.2138/gselements.15.4.259.

770 Gaillardet, J., Dupré, B., and Allègre, C.J., 1999, Geochemistry of large river suspended sediments: silicate
771   weathering or recycling tracer? Geochimica et Cosmochimica Acta, v. 63, p. 4037–4051,
772   doi:10.1016/S0016-7037(99)00307-5.

773 Gaitan, C.E., Pucéat, E., Pellenard, P., Blondet, J., Bayon, G., Adatte, T., Israel, C., Robin, C., and Guillocheau,
774   F., 2023, Late Cretaceous erosion and chemical weathering record in the offshore Cape Basin: Source-
775   to-sink system from Hf Nd isotopes and clay mineralogy: Marine Geology, v. 466, p. 107187,
776   doi:10.1016/j.margeo.2023.107187.

777 Gallagher, T.M., Cacciatore, C.G., and Breecker, D.O., 2019, Interpreting the Difference in Magnitudes of
778   PETM Carbon Isotope Excursions in Paleosol Carbonate and Organic Matter: Oxidation of Methane in
779   Soils Versus Elevated Soil Respiration Rates: Paleoceanography and Paleoclimatology, v. 34, p. 2113–
780   2128, doi:10.1029/2019PA003596.

781 Gawenda, P., Winkler, W., Schmitz, B., and Adatte, T., 1999, Climate and bioproductivity control on carbonate
782   turbidite sedimentation (Paleocene to earliest Eocene, Gulf of Biscay, Zumaia, Spain): Journal of
783   Sedimentary Research, v. 69, p. 1253–1261, doi:10.2110/jsr.69.1253.

784 Gibbs, 1977, Clay Mineral Segregation in the Marine Environment: SEPM Journal of Sedimentary Research, v.
785   Vol. 47, doi:10.1306/212F713A-2B24-11D7-8648000102C1865D.

786 Goddéris, Y., Donnadieu, Y., Tombozafy, M., and Dessert, C., 2008, Shield effect on continental weathering:
787   Implication for climatic evolution of the Earth at the geological timescale: Geoderma, v. 145, p. 439–
788   448, doi:10.1016/j.geoderma.2008.01.020.

789 Gómez-Gras, D., Roigé, M., Fondevilla, V., Oms, O., Boya, S., and Remacha, E., 2016, Provenance constraints
790   on the Tremp Formation paleogeography (southern Pyrenees): Ebro Massif VS Pyrenees sources:
791   Cretaceous Research, v. 57, p. 414–427, doi:10.1016/j.cretres.2015.09.010.

792 Gutjahr, M., Frank, M., Stirling, C.H., Klemm, V., Van De Flierdt, T., and Halliday, A.N., 2007, Reliable
793   extraction of a deepwater trace metal isotope signal from Fe–Mn oxyhydroxide coatings of marine
794   sediments: Chemical Geology, v. 242, p. 351–370, doi:10.1016/j.chemgeo.2007.03.021.

795 Hessler, A.M., Zhang, J., Covault, J., and Ambrose, W., 2017, Continental weathering coupled to Paleogene
796   climate changes in North America: Geology, v. 45, p. 911–914, doi:10.1130/G39245.1.

797 Hilton, R.G., 2023, Earth's persistent thermostat: Science, v. 379, p. 329–330, doi:10.1126/science.adf3379.

798 Jaimes-Gutierrez, R., Adatte, T., Pucéat, E., Vennemann, T., Prieur, M., Wild, A.L., Khozyem, H., Vaucher, R.,
799   and Castelltort, S., 2024, Deciphering Paleocene-Eocene Thermal Maximum Climatic Dynamics:
800   Insights From Oxygen and Hydrogen Isotopes in Clay Minerals of Paleosols From the Southern
801   Pyrenees: Paleoceanography and Paleoclimatology, v. 39, p. e2024PA004858,
802   doi:10.1029/2024PA004858.

803 Jaimes-Gutierrez, R., Vimpere, L., Wilson, D.J., Blaser, P., Adatte, T., Sahoo, S., and Castelltort, S., 2025a,
804   Lithium isotopes reveal enhanced weathering fluxes in North America during the Paleocene–Eocene
805   Thermal Maximum: Geology, doi:https://doi.org/10.1130/G53708.1.

806 Jones, M.T. et al., 2023, Tracing North Atlantic volcanism and seaway connectivity across the Paleocene–
807   Eocene Thermal Maximum (PETM): Climate of the Past, v. 19, p. 1623–1652, doi:10.5194/cp-19-
808   1623-2023.

809 Kennett, J.P., and Stott, L.D., 1991, Abrupt deep-sea warming, palaeoceanographic changes and benthic
810   extinctions at the end of the Palaeocene: Nature, v. 353, p. 225–229, doi:10.1038/353225a0.

811 Khozyem, H.M.A., 2013, Sedimentology, geochemistry and mineralogy of the Paleocene Eocene Thermal
812   Maximum (PETM): Sediment records from Egypt, India and Spain [Doctoral Dissertation]: Université
813   de Lausanne, 195 p.

814 Kısakűrek, B., James, R.H., and Harris, N.B.W., 2005, Li and δ7Li in Himalayan rivers: Proxies for silicate
815   weathering? Earth and Planetary Science Letters, v. 237, p. 387–401, doi:10.1016/j.epsl.2005.07.019.

816 Krause, A.J., Sluijs, A., Van Der Ploeg, R., Lenton, T.M., and Pogge Von Strandmann, P.A.E., 2023, Enhanced
817   clay formation key in sustaining the Middle Eocene Climatic Optimum: Nature Geoscience, v. 16, p.
818   730–738, doi:10.1038/s41561-023-01234-y.

819 Kump, L.R., and Arthur, M.A., 1997, Global Chemical Erosion during the Cenozoic: Weatherability Balances
820   the Budgets, *in* Ruddiman, W.F. ed., Tectonic Uplift and Climate Change, Boston, MA, Springer US,
821   p. 399–426, doi:10.1007/978-1-4615-5935-1_18.

822 Kump, L.R., Brantley, S.L., and Arthur, M.A., 2000, Chemical Weathering, Atmospheric CO_2, and Climate:
823   Annual Review of Earth and Planetary Sciences, v. 28, p. 611–667,
824   doi:10.1146/annurev.earth.28.1.611.

825 Li, G., and West, A.J., 2014, Evolution of Cenozoic seawater lithium isotopes: Coupling of global denudation
826   regime and shifting seawater sinks: Earth and Planetary Science Letters, v. 401, p. 284–293,
827   doi:10.1016/j.epsl.2014.06.011.

828 Liu, C.-Y., Wilson, D.J., Hathorne, E.C., Xu, A., and Pogge Von Strandmann, P.A.E., 2023, The influence of
829   river-derived particles on estuarine and marine elemental cycles: Evidence from lithium isotopes:
830   Geochimica et Cosmochimica Acta, v. 361, p. 183–199, doi:10.1016/j.gca.2023.08.015.

831 Maffre, P., Goddéris, Y., Vigier, N., Moquet, J.-S., and Carretier, S., 2020, Modelling the riverine δ7Li
832   variability throughout the Amazon Basin: Chemical Geology, v. 532, p. 119336,
833   doi:10.1016/j.chemgeo.2019.119336.

834 Maher, K., and Von Blanckenburg, F., 2023, The circular nutrient economy of terrestrial ecosystems and the
835   consequences for rock weathering: Frontiers in Environmental Science, v. 10, p. 1066959,
836   doi:10.3389/fenvs.2022.1066959.

837 Mattauer, M., and Henry, J., 1974, Pyrenees: Special Publications, v. 4, no.1, p. 3–21.

838 McInerney, F.A., and Wing, S.L., 2011, The Paleocene-Eocene Thermal Maximum: A Perturbation of Carbon
839   Cycle, Climate, and Biosphere with Implications for the Future: Annual Review of Earth and Planetary
840   Sciences, v. 39, p. 489–516, doi:10.1146/annurev-earth-040610-133431.

841 Meunier, A., 2005, Clays: Berlin ; New York, Springer, 472 p.

842 Misra, S., and Froelich, P.N., 2012, Lithium Isotope History of Cenozoic Seawater: Changes in Silicate
843   Weathering and Reverse Weathering: Science, v. 335, p. 818–823, doi:10.1126/science.1214697.

844 Moore, D.M., and Reynolds, R.C., 1992, Moore, Reynolds 1997_X-Ray Diffraction.pdf: New York, Oxford
845   University Press, 401 p.

846 Moulton, K.L., West, J., and Berner, R.A., 2000, Solute flux and mineral mass balance approaches to the
847   quantification of plant effects on silicate weathering: v. 300, p. 539–570.

848 Muñoz, J.A., 1992, Evolution of a continental collision belt: ECORS-Pyrenees crustal balanced cross-section, *in*
849   McClay, K.R. ed., Thrust Tectonics, Dordrecht, Springer Netherlands, p. 235–246, doi:10.1007/978-
850   94-011-3066-0_21.

851 Murray, J., and Jagoutz, O., 2024, Palaeozoic cooling modulated by ophiolite weathering through organic
852   carbon preservation: Nature Geoscience, v. 17, p. 88–93, doi:10.1038/s41561-023-01342-9.

853 Pistiner, J.S., and Henderson, G.M., 2003, Lithium-isotope fractionation during continental weathering
854   processes: Earth and Planetary Science Letters, v. 214, p. 327–339, doi:10.1016/S0012-
855   821X(03)00348-0.

856 Pogge von Strandmann, P.A.E., Cosford, L.R., Liu, C.-Y., Liu, X., Krause, A.J., Wilson, D.J., He, X., McCoy-
857   West, A.J., Gislason, S.R., and Burton, K.W., 2023, Assessing hydrological controls on the lithium
858   isotope weathering tracer: Chemical Geology, v. 642, p. 121801, doi:10.1016/j.chemgeo.2023.121801.

859 Pogge von Strandmann, P.A.E.P.V., Dellinger, M., and West, A.J., 2021a, Lithium Isotopes: A Tracer of Past
860   and Present Silicate Weathering: Cambridge University Press, doi:10.1017/9781108990752.

861 Pogge Von Strandmann, P.A.E., Fraser, W.T., Hammond, S.J., Tarbuck, G., Wood, I.G., Oelkers, E.H., and
862   Murphy, M.J., 2019, Experimental determination of Li isotope behaviour during basalt weathering:
863   Chemical Geology, v. 517, p. 34–43, doi:10.1016/j.chemgeo.2019.04.020.

864 Pogge von Strandmann, P.A.E., Jenkyns, H.C., and Woodfine, R.G., 2013, Lithium isotope evidence for
865   enhanced weathering during Oceanic Anoxic Event 2: Nature Geoscience, v. 6, p. 668–672,
866   doi:10.1038/ngeo1875.

867 Pogge von Strandmann, P.A.E., Jones, M.T., West, A.J., Murphy, M.J., Stokke, E.W., Tarbuck, G., Wilson,
868   D.J., Pearce, C.R., and Schmidt, D.N., 2021b, Lithium isotope evidence for enhanced weathering and
869   erosion during the Paleocene-Eocene Thermal Maximum: Science Advances, v. 7, p. eabh4224,
870   doi:10.1126/sciadv.abh4224.

871 Pogge von Strandmann, P.A.E., Kasemann, S.A., and Wimpenny, J.B., 2020, Lithium and Lithium Isotopes in
872   Earth's Surface Cycles: v. 16, p. 253–258, doi:10.2138/gselements.16.4.253.

873 Porder, S., 2019, How Plants Enhance Weathering and How Weathering is Important to Plants: Elements, v. 15,
874   p. 241–246, doi:10.2138/gselements.15.4.241.

875 Presti, M., and Michalopoulos, P., 2008, Estimating the contribution of the authigenic mineral component to the
876   long-term reactive silica accumulation on the western shelf of the Mississippi River Delta: Continental
877   Shelf Research, v. 28, p. 823–838, doi:10.1016/j.csr.2007.12.015.

878 Prieur, M. et al., 2025, Climate Control on Erosion: Evolution of Sediment Flux From Mountainous Catchments
879   During a Global Warming Event, PETM, Southern Pyrenees, Spain: Geophysical Research Letters, v.
880   52, p. e2024GL112404, doi:10.1029/2024GL112404.

881 Prieur, M., Whittaker, A.C., Nuriel, P., Jaimes-Gutierrez, R., Garzanti, E., Roigé, M., Sømme, T.O.,
882   Schlunegger, F., and Castelltort, S., 2024, Fingerprinting enhanced floodplain reworking during the
883   Paleocene–Eocene Thermal Maximum in the Southern Pyrenees (Spain): Implications for channel
884   dynamics and carbon burial: Geology, v. 52, p. 651–655, doi:10.1130/G52180.1.

885 Puigdefbregas, C., and Souquet, P., 1986, Tecto-sedimentary cycles and depositional sequences of the Mesozoic
886   and Tertiary from the Pyrenees: v. 129, p. 173–203.

887 Pujalte, V., Baceta, J.I., and Schmitz, B., 2015, A massive input of coarse-grained siliciclastics in the Pyrenean
888   Basin during the PETM: the missing ingredient in a coeval abrupt change in hydrological regime:
889   Climate of the Past, v. 11, p. 1653–1672, doi:10.5194/cp-11-1653-2015.

890 Pujalte, V., Robador, A., Aitor Payros, and Samsó, J.M., 2016, A siliciclastic braid delta within a lower
891   Paleogene carbonate platform (Ordesa-Monte Perdido National Park, southern Pyrenees, Spain):
892   Record of the Paleocene–Eocene Thermal Maximum perturbation: Palaeogeography,
893   Palaeoclimatology, Palaeoecology, v. 459, p. 453–470, doi:10.1016/j.palaeo.2016.07.029.

894 Pujalte, V., and Schmitz, B., 2005, Revisión de la estratigrafía del Grupo Tremp («Garumniense», Cuenca de
895   Tremp-Graus, Pirineos meridionales):

896   Pujalte, V., Schmitz, B., and Baceta, J.I., 2014, Sea-level changes across the Paleocene–Eocene interval in the
897   Spanish Pyrenees, and their possible relationship with North Atlantic magmatism: Palaeogeography,
898   Palaeoclimatology, Palaeoecology, v. 393, p. 45–60, doi:10.1016/j.palaeo.2013.10.016.

899   Pujalte, V., Schmitz, B., Baceta, J.I., Orue-Etxebarria, X., Bernaola, G., Dinarès-Turell, J., Payros, A.,
900   Apellaniz, E., and Caballero, F., 2009, Correlation of the Thanetian-Ilerdian turnover of larger
901   foraminifera and the Paleocene-Eocene thermal maximum: confirming evidence from the Campo area
902   (Pyrenees, Spain): Geologica Acta, v. 7.

903   Ramos, E.J. et al., 2024, Competition or collaboration: Clay formation sets the relationship between silicate
904   weathering and organic carbon burial in soil: Earth and Planetary Science Letters, v. 628, p. 118584,
905   doi:10.1016/j.epsl.2024.118584.

906   Ramos, E.J. et al., 2022, Swift Weathering Response on Floodplains During the Paleocene-Eocene Thermal
907   Maximum: Geophysical Research Letters, v. 49, doi:10.1029/2021GL097436.

908   Raymo, M.E., and Ruddiman, W.F., 1992, Tectonic forcing of late Cenozoic climate: Nature, v. 359, p. 117–
909   122, doi:10.1038/359117a0.

910   Riebe, C.S., Kirchner, J.W., and Finkel, R.C., 2004, Erosional and climatic effects on long-term chemical
911   weathering rates in granitic landscapes spanning diverse climate regimes: Earth and Planetary Science
912   Letters, v. 224, p. 547–562, doi:10.1016/j.epsl.2004.05.019.

913   Roest, W.R., and Srivastava, S.P., 1991, Kinematics of the plate boundaries between Eurasia, Iberia, and Africa
914   in the North Atlantic from the Late Cretaceous to the present: Geology, v. 19, p. 613,
915   doi:10.1130/0091-7613(1991)019<0613:KOTPBB>2.3.CO;2.

916   Rosenbaum, G., Lister, G.S., and Duboz, C., 2002, Reconstruction of the tectonic evolution of the western
917   Mediterranean since the Oligocene: Journal of the Virtual Explorer, v. 08,
918   doi:10.3809/jvirtex.2002.00053.

919   Roure, F., Choukroune, P., Berastegui, X., Munoz, J.A., Villien, A., Matheron, P., Bareyt, M., Seguret, M.,
920   Camara, P., and Deramond, J., 1989, Ecors deep seismic data and balanced cross sections: Geometric
921   constraints on the evolution of the Pyrenees: Tectonics, v. 8, p. 41–50, doi:10.1029/TC008i001p00041.

922   Rush, W.D., Kiehl, J.T., Shields, C.A., and Zachos, J.C., 2021, Increased frequency of extreme precipitation
923   events in the North Atlantic during the PETM: Observations and theory: Palaeogeography,
924   Palaeoclimatology, Palaeoecology, v. 568, p. 110289, doi:10.1016/j.palaeo.2021.110289.

925   Rush, W., Zachos, J., Blackburn, T., and Pogge Von Strandmann, P.A.E., 2025, Continuous Sediment Sourcing
926   and Changes in Weathering During the PETM in the Salisbury Embayment: Paleoceanography and
927   Paleoclimatology, v. 40, p. e2025PA005116, doi:10.1029/2025PA005116.

928   Schmitz, B., and Pujalte, V., 2007, Abrupt increase in seasonal extreme precipitation at the Paleocene-Eocene
929   boundary: Geology, v. 35, p. 215, doi:10.1130/G23261A.1.

930   Schmitz, B., and Pujalte, V., 2003, Sea-level, humidity, and land-erosion records across the initial Eocene
931   thermal maximum from a continental-marine transect in northern Spain: Geology, v. 31, p. 689,
932   doi:10.1130/G19527.1.

933   Schmitz, B., Pujalte, V., and Nunhez-Betelu, K., 2001, Climate and sea-level perturbations during the Initial
934   Eocene Thermal Maximum: evidence from siliciclastic units in the Basque Basin (Ermua, Zumaia and
935   Trabakua Pass), northern Spain: Palaeogeography, Palaeoclimatology, Palaeoecology 165, p. 299–320.

936   Spangenberg, J.E., 2006, Hydrocarbon Biomarkers in the Topla-Mežica Zinc-Lead Deposits, Northern
937   Karavanke/Drau Range, Slovenia: Paleoenvironment at the Site of Ore Formation:

938   Spangenberg, J.E., and Zufferey, V., 2019, Carbon isotope compositions of whole wine, wine solid residue, and
939   wine ethanol, determined by EA/IRMS and GC/C/IRMS, can record the vine water status—a

940 comparative reappraisal: Analytical and Bioanalytical Chemistry, v. 411, p. 2031–2043,
941   doi:10.1007/s00216-019-01625-4.

942 Środoń, J., 2001, Quantitative X-Ray Diffraction Analysis of Clay-Bearing Rocks from Random Preparations:
943   Clays and Clay Minerals, v. 49, p. 514–528, doi:10.1346/CCMN.2001.0490604.

944 Tanaka, T. et al., 2000, JNdi-1: a neodymium isotopic reference in consistency with LaJolla neodymium:
945   Chemical Geology, v. 168, p. 279–281, doi:10.1016/S0009-2541(00)00198-4.

946 Teixell, A., Labaume, P., and Lagabrielle, Y., 2016, The crustal evolution of the west-central Pyrenees revisited:
947   Inferences from a new kinematic scenario: Comptes Rendus. Géoscience, v. 348, p. 257–267,
948   doi:10.1016/j.crte.2015.10.010.

949 Thiry, M., 2000, Palaeoclimatic interpretation of clay minerals in marine deposits: an outlook from the
950   continental origin: Earth-Science Reviews, v. 49, p. 201–221, doi:10.1016/S0012-8252(99)00054-9.

951 Tofelde, S., Bernhardt, A., Guerit, L., and Romans, B.W., 2021, Times Associated With Source-to-Sink
952   Propagation of Environmental Signals During Landscape Transience: Frontiers in Earth Science, v. 9,
953   p. 628315, doi:10.3389/feart.2021.628315.

954 Tremblin, M. et al., 2022, Mercury enrichments of the Pyrenean foreland basins sediments support enhanced
955   volcanism during the Paleocene-Eocene thermal maximum (PETM): Global and Planetary Change, v.
956   212, p. 103794, doi:10.1016/j.gloplacha.2022.103794.

957 Velde, B., and Meunier, A., 2008, The Origin of Clay Minerals in Soils and Weathered Rocks: Berlin,
958   Heidelberg, Springer Berlin Heidelberg, doi:10.1007/978-3-540-75634-7.

959 Vigier, N., Decarreau, A., Millot, R., Carignan, J., Petit, S., and France-Lanord, C., 2008, Quantifying Li
960   isotope fractionation during smectite formation and implications for the Li cycle: Geochimica et
961   Cosmochimica Acta, v. 72, p. 780–792, doi:10.1016/j.gca.2007.11.011.

962 Vimpere, L. et al., 2023, Carbon isotope and biostratigraphic evidence for an expanded Paleocene–Eocene
963   Thermal Maximum sedimentary record in the deep Gulf of Mexico: Geology, doi:10.1130/G50641.1.

964 Walker, J.C.G., Hays, P.B., and Kasting, J.F., 1981, A negative feedback mechanism for the long-term
965   stabilization of Earth's surface temperature: Journal of Geophysical Research: Oceans, v. 86, p. 9776–
966   9782, doi:10.1029/JC086iC10p09776.

967 Wei, G.-Y., Pohl, A., Jiang, S., Zhang, H., Wang, W., A. E. Pogge Von Strandmann, P., Maffre, P., Xiong, G.,
968   Shen, S., and Zhang, F., 2025, Changes in continental weathering regimes inhibited global marine
969   deoxygenation during the Paleocene-Eocene thermal maximum: Nature Communications, v. 16, p.
970   9163, doi:10.1038/s41467-025-64217-0.

971 Weis, D., Kieffer, B., Maerschalk, C., Pretorius, W., and Barling, J., 2005, High-precision Pb-Sr-Nd-Hf isotopic
972   characterization of USGS BHVO-1 and BHVO-2 reference materials: Geochemistry, Geophysics,
973   Geosystems, v. 6, p. 2004GC000852, doi:10.1029/2004GC000852.

974 West, A., Galy, A., and Bickle, M., 2005, Tectonic and climatic controls on silicate weathering: Earth and
975   Planetary Science Letters, v. 235, p. 211–228, doi:10.1016/j.epsl.2005.03.020.

976 Westerhold, T., Röhl, U., McCarren, H.K., and Zachos, J.C., 2009, Latest on the absolute age of the Paleocene–
977   Eocene Thermal Maximum (PETM): New insights from exact stratigraphic position of key ash layers
978   +19 and −17: Earth and Planetary Science Letters, v. 287, p. 412–419, doi:10.1016/j.epsl.2009.08.027.

979 Wilson, D.J., Pogge von Strandmann, P.A.E., White, J., Tarbuck, G., Marca, A.D., Atkinson, T.C., and Hopley,
980   P.J., 2021, Seasonal variability in silicate weathering signatures recorded by Li isotopes in cave drip-
981   waters: Geochimica et Cosmochimica Acta, v. 312, p. 194–216, doi:10.1016/j.gca.2021.07.006.

982 Winnick, M.J., Druhan, J.L., and Maher, K., 2022, Weathering intensity and lithium isotopes: A reactive
983   transport perspective: American Journal of Science, v. 322, p. 647–682, doi:10.2475/05.2022.01.

984 Wise, S.W., Smellie, J., Aghib, F., Jarrard, R., and Krissek, L., 2001, Authigenic Smectite Clay Coats in CRP-3
985   Drillcore, Victoria Land Basin, Antarctica, as a Possible Indicator of Fluid Flow: A Progress Report: ,
986   p. 281–298.

987 Xu, Z., Li, T., Li, G., Hedding, D.W., Wang, Y., Gou, L.-F., Zhao, L., and Chen, J., 2022, Lithium isotopic
988   composition of soil pore water: Responses to evapotranspiration: Geology, v. 50, p. 194–198,
989   doi:10.1130/G49366.1.

990 Zachos, J.C., Dickens, G.R., and Zeebe, R.E., 2008, An early Cenozoic perspective on greenhouse warming and
991   carbon-cycle dynamics: Nature, v. 451, p. 279–283, doi:10.1038/nature06588.

992 Zachos, J.C., Wara, M.W., Bohaty, S., Delaney, M.L., Petrizzo, M.R., Brill, A., Bralower, T.J., and Premoli-
993   Silva, I., 2003, A Transient Rise in Tropical Sea Surface Temperature During the Paleocene-Eocene
994   Thermal Maximum: Science, v. 302, p. 1551–1554, doi:10.1126/science.1090110.

995 Zeebe, R.E., Ridgwell, A., and Zachos, J.C., 2016, Anthropogenic carbon release rate unprecedented during the
996   past 66 million years: Nature Geoscience, v. 9, p. 325–329, doi:10.1038/ngeo2681.

997 Zhang, F., Dellinger, M., Hilton, R.G., Yu, J., Allen, M.B., Densmore, A.L., Sun, H., and Jin, Z., 2022,
998   Hydrological control of river and seawater lithium isotopes: Nature Communications, v. 13, p. 3359,
999   doi:10.1038/s41467-022-31076-y.

1000